PAPER • OPEN ACCESS

Effects of strong spin-orbit coupling on Shiba states from magnetic adatoms using first-principles theory

To cite this article: Kyungwha Park *et al* 2023 *New J. Phys.* **25** 033022

View the article online for updates and enhancements.

New Journal of Physics

The open access journal at the forefront of physics

PAPER

Effects of strong spin-orbit coupling on Shiba states from magnetic adatoms using first-principles theory

Kyungwha Park[1],* , Bendeguz Nyari[2,3] , Andras Laszloffy[4] , Laszlo Szunyogh[2,3] and Balazs Ujfalussy[4,*]

[1] Department of Physics, Virginia Tech, Blacksburg, VA 24061, United States of America
[2] Department of Theoretical Physics, Institute of Physics, Budapest University of Technology and Economics, Müegyetem rkp. 3, H-1111 Budapest, Hungary
[3] ELKH-BME Condensed Matter Research Group, Budapest University of Technology and Economics, Müegyetem rkp. 3, H-1111 Budapest, Hungary
[4] Wigner Research Centre for Physics, PO Box 49, H-1525 Budapest, Hungary
* Authors to whom any correspondence should be addressed.

E-mail: kyungwha@vt.edu and ujfalussy.balazs@wigner.hu

Abstract

Magnetic impurities at surfaces of superconductors can induce bound states referred to as Yu–Shiba–Rusinov states (i.e. Shiba states) within superconducting (SC) gaps. For superconductors with strong spin–orbit coupling (SOC), Shiba states arising from even single magnetic adatoms are too complex to be fully understood using effective models alone because SOC cannot be treated perturbatively and multiple orbitals are strongly mixed with spin projections. Here we investigate Shiba states of single magnetic adatoms at the surface of strongly spin-orbit coupled SC Pb, by solving the fully relativistic Dirac–Bogoliubov–de Gennes equations using multiple scattering Green's function methods. For Fe and Co adatoms on Pb(110), we show that the Shiba states are better characterized by total angular momentum, J, and its projections on the z axis, m_J. As a hallmark of the SOC effect, the Shiba states show a strong dependence of the orientation of the adatom moment. As the orientation of the Fe/Co moment changes, the deepest Shiba states merge at zero energy. This zero-energy state disappears with an additional non-magnetic adatom next to the magnetic adatom, although the other Shiba states unchange. For a Mn adatom on Pb, our Shiba states overall agree with experiments. The characteristics of our Shiba states are also observed with the similar energies and characters in the experiments. The deepest Shiba states that we compute, however, do not appear as close to the Fermi level as the experimental data. It would be interesting to compute the Shiba states with continuously varying vertical distances of the Mn adatom from the surface or with varying the charge state of the adatom, and to calculate the spatial dependence of the spectral density. Our findings will be also useful for understanding of Shiba states for dimers and longer spin chains on the Pb surface considering noncollinear magnetic structures in them.

1. Introduction

When magnetic impurities are present at surfaces of superconductors, quasiparticle excitations referred to as Yu–Shiba–Rusinov states [1–3] (i.e. Shiba states) can appear within superconducting (SC) gaps. Spin-up and spin-down electrons in forming the Cooper pairs experience different exchange interaction with the magnetic moment of the impurity. This interaction weakens or even breaks the bonding between the Cooper pair elements, which results in states within the SC gap.

These excitations were studied in various pairing symmetries of SC states [4–7]. Being able to calculate the properties of Shiba states and to describe their formation conditions has been shown to be pivotal in understanding of topological end modes [8–19] in the presence of spin–orbit coupling (SOC) or spiral magnetic order. Very recently, a scanning tunneling microscopy/spectroscopy experiment [20] showed

zero-energy end modes in dilute spin chains in proximity to an *s*-wave SC substrate. These end modes turned out to be topologically trivial Shiba states. Furthermore, Shiba states were proven to be very useful to probe magnetic nanostructures at surfaces with high resolution by using SC STM tips [21].

In many theoretical reports, these excitations (i.e. Shiba states) have been studied using single-orbital spin $S = 1/2$ effective models in the absence of SOC [1–4, 9, 22–26]. This approach does not capture major properties of Shiba states arising from transition-metal adatoms and chains, or Shiba states when the SC substrates have strong SOC. Recently, characteristics of Shiba states have been studied using a multi-orbital effective model consisting of five $l = 2$ orbitals in the presence of crystal field splitting without SOC [27].

In an effective-model approach for Shiba states, SOC was considered at different levels in different models [8, 11, 28–32]. In [11], within a single-orbital model, Rashba SOC was included at the perturbative limit in ferromagnetic chains but not in the SC substrate, and the properties of Shiba states and Majorana zero-energy modes are discussed. In [28], Rashba SOC was taken into account in the SC substrate using a model comprising three $l = 1$ orbitals. It was found that the positions of Shiba states within the SC gap change as a function of SOC strength and direction of the magnetic moment [28]. In [29], SOC was inherently considered in terms of magnetic anisotropy for transition-metal magnetic impurities with high spin $S > 1/2$. This study showed phase diagrams of the number of Shiba states and the projection of the total spin as a function of pairing strength and uniaxial magnetic anisotropy parameter. All of the aforementioned model Hamiltonian studies are neither self-consistent calculations nor based on realistic parameters for the magnetic impurities and the SC substrates.

In order to consider the effects of SOC and multi-orbitals on Shiba states within self-consistent calculations with realistic band structures, we previously developed relativistic first-principles methods [33], and applied them to Shiba states arising from single Mn impurities and Mn dimers at a semi-infinite Nb substrate [33]. Within this methodology, we were able to characterize multiple Shiba states and showed that the splitting of Shiba states from ferromagnetic Mn dimers quantitatively agrees with experimental data from [34]. The first-principles study in [33] differs from the recent study using a similar first-principles approach [35], where quasiparticle excitations were studied for single magnetic impurities embedded deeply inside three-dimensional bulk Pb without SOC.

In this work, we investigate characteristics of Shiba states from single transition-metal magnetic adatoms (Fe, Co, Mn) on a Pb substrate as well as resonances from the neighboring Pb atoms, by performing first-principles calculations including SOC in the SC state. In our simulations, *s*, *p*, and *d* orbitals of the magnetic adatoms and the band structure of Pb are all included. We find that each Shiba state of *d*-orbital character exhibits strong coupling among different $3d$ orbitals and spin-up and spin-down projections due to strong SOC of the Pb substrate, in contrast to a SOC-free or weak-SOC case where each Shiba state corresponds to an individual $3d$ orbital. Therefore, we characterize Shiba states using the total angular momentum J and its projection along the magnetic moment direction m_J, and show unique features of Shiba states in which SOC-induced spin mixing is strong. We study how the Shiba states are affected when the orientation of the adatom moment changes. We also discuss why the Shiba states from the Fe and Co adatoms appear deep inside the SC gap, and compare our results with available experimental data.

2. Methods

Regarding our first-principles calculations of the normal and the SC states, we use the methods developed in [33]. Nyári *et al* [33] summarizes all the essential formulas and necessary procedures to solve the Dirac–Bogoliubov–de Gennes (DBdG) equation based on first-principles multiple scattering theory for embedded magnetic impurities on surfaces of superconductors. Therefore, we here briefly describe only the relevant details of the implementation for systems of interest.

First we perform first-principles calculations of bulk Pb and a *semi-infinite* Pb slab in the normal state with the experimental lattice constant (4.95 Å [36]) using the fully relativistic screened Korringa–Kohn–Rostoker (SKKR) Green's function method [33, 37] within Kohn–Sham-Dirac density functional theory in the atomic sphere approximation. For the Pb(110) and Pb(001) slab calculations, we consider four Pb atomic layers and four vacuum layers in the interface region treated self-consistently. For the Pb(111) slab calculation, we consider six Pb atomic layers and three vacuum layers in the interface region. The local spin density approximation [38] is used for exchange-correlation functional. Relativistic effects are taken into account in terms of the Kohn–Sham–Dirac equation. Scaling of the SOC is employed as proposed by Ebert *et al* [39]. In all calculations unless specified otherwise, 2450 *k* points are used with an orbital angular momentum cutoff of $l_{max} = 2$ in the irreducible wedge of the two-dimensional Brillouin zone. The global *x* axis is along the [$\bar{1}$10] direction, and the global *y* axis is along the [001] direction of Pb(110) surface (see figure 1(a)). The global *z* axis is normal to the surface. The Fermi level of bulk Pb and vacuum potential of the Pb(110) slab are determined from self-consistent calculations.

We employ the embedded cluster method [40] self-consistently within the SKKR formalism to a single Fe, Co, or Mn magnetic adatom at the surface of the semi-infinite Pb(110) slab, as well as a Mn adatom on Pb(111) and Pb(001) slabs. For the Pb(110) slab, the Fe, Co, or Mn atom is located at the hollow site of the surface with the vertical distance of 1.75 Å from the Pb surface, unless specified otherwise. This distance is an interlayer distance of a pristine Pb(110) slab. Similarly, for the Pb(111) and P(001) slabs, the Mn adatom is located at the hollow site with the vertical distances of 2.86 and 2.48 Å, respectively. In the embedded cluster method, the system is divided into an impurity cluster (IC) and a host. The former consists of the magnetic impurity atom, neighboring Pb atoms, and surrounding empty spheres which represent vacuum layers, while the latter corresponds to the rest of the Pb atoms. Considering only nearest neighboring Pb atoms and vacuum sites to the magnetic adatom, we use a 13-site IC. Following the similar logic, for a Fe–S impurity, we use a 22-site IC, where sulfur (S) is located right next to the Fe site along the *x* axis in the same atomic layer. When the Fe impurity site is located at the Pb surface layer, we consider a 13-site IC. We confirm that our results do not change with a further increase of the IC size. Then using the SKKR electrostatic potential of the bare semi-infinite Pb slab, we compute the potential of the IC self-consistently in the normal state. Normal-state impurity density of states (DOS) plots are computed from Bloch spectral functions with 1250 *k* points, using a broadening of 1.0 mRy and an energy resolution of 5.0 mRy.

The converged normal-state potentials are used to solve the DBdG equations for the Green's function matrix [33, 37, 41]. We use the pairing potential Δ of bulk and interface Pb layers as the experimental SC gap of bulk Pb, 0.1 mRy (=1.36 meV) [36], with *s*-wave pairing symmetry, while the pairing potential of the Fe, Co, or Mn atom is set to zero. The DOS $\rho_I(\epsilon)$ of atom *I*, i.e. local DOS (LDOS), at energy ϵ in the IC is computed non-self consistently from the electron- and hole-components of the Green's function matrix $G^{ee}_{L,\sigma;L,\sigma}$ and $G^{hh}_{L,\sigma;L,\sigma}$ with a broadening of 0.5 μRy and an energy resolution of 1 μRy:

$$\rho_I(\epsilon) = -\frac{1}{\pi}\mathrm{Im}\int_{\mathrm{WS}} d^3r \sum_{\sigma} \mathrm{Tr}_L[G^{ee}_{I;L,\sigma;L,\sigma}(\epsilon,\mathbf{r},\mathbf{r}) + G^{hh}_{I;L,\sigma;L,\sigma}(\epsilon,\mathbf{r},\mathbf{r})], \tag{1}$$

where *L* and σ are orbital and spin indices, respectively. Here the integral runs over an atomic sphere around atom *I* with its Wigner–Seitz radius. Spin-decomposed DOS is calculated from projection of the total LDOS onto spin-up and down components along the rotating magnetic moment direction. Orbital characters are obtained from the global coordinates which do not change with the direction of the magnetic moment. We also decompose the SC-state LDOS into $|J, m_J\rangle$ states using the $\{\kappa, \mu\}$ representation [41], where κ is the spin-orbit quantum number and $\mu = m_J$, when the magnetic moment is oriented along the *z* axis.

3. Fe adatom on Pb(110)

3.1. Properties of the normal state

We investigate properties of the normal state of the Fe adatom at the hollow site above the Pb surface (figure 1(a)) since they provide important insights into properties of Shiba states in the SC state. Let us first discuss the case that the Fe magnetic moment vector points normal to the surface (i.e. along the *z* axis). In this case, we obtain the Fe spin and orbital moments of 3.518 and 0.906 μ_B, respectively, which significantly differ from those of an isolated Fe atom, i.e. 4.0 and 2.0 μ_B, respectively. This is due to substantial charge transfer from the semi-infinite Pb bulk to the Fe adatom as well as orbital hybridization between them. Furthermore, small magnetic moments are induced in Pb atoms close to the Fe adatom. Each of the nearest-neighboring Pb atoms has a spin moment of 0.026 μ_B with a direction opposite to the Fe spin moment. The rest of the Pb atoms in the IC have spin moments of an order of 0.001 μ_B or less.

Figure 1(b) shows spin-decomposed LDOS of the Fe adatom in the normal state. The Fe spin-up and spin-down LDOS spectra are broadened due to orbital hybridization between the Fe adatom and the Pb substrate. The energy difference between the spin-up DOS peak and spin-down DOS peak is about 0.212 Ry. The position of the spin-down DOS peak is slightly above the Fermi level E_F. Considering the large peak-to-peak separation between the spin-up and spin-down DOS compared to their linewidths, we observe that the Fe spin-up LDOS is almost fully occupied and that the LDOS at E_F predominantly has spin-down character. Figure 1(d) shows the orbital-decomposed spin-down LDOS of the Fe adatom. All *d* orbitals of the Fe adatom substantially contribute to the LDOS at E_F, although $d_{x^2-y^2}$ orbital has the largest contribution. The comparable *d* orbitals are expected to strongly couple to the spin via hybridization with the strongly spin-orbit coupled Pb substrate. In addition to the *d* orbitals, there exists small LDOS of *s*- and *p*-orbital character with unequal spin-up and spin-down weights at the Fermi level. These features along with the charge-transfer effect may be difficult to include in an effective model to study Shiba states.

One important consequence of SOC is that electronic and magnetic properties can be affected by the direction of the Fe magnetic moment. We first discuss rotations of the magnetic moment by angle θ from the
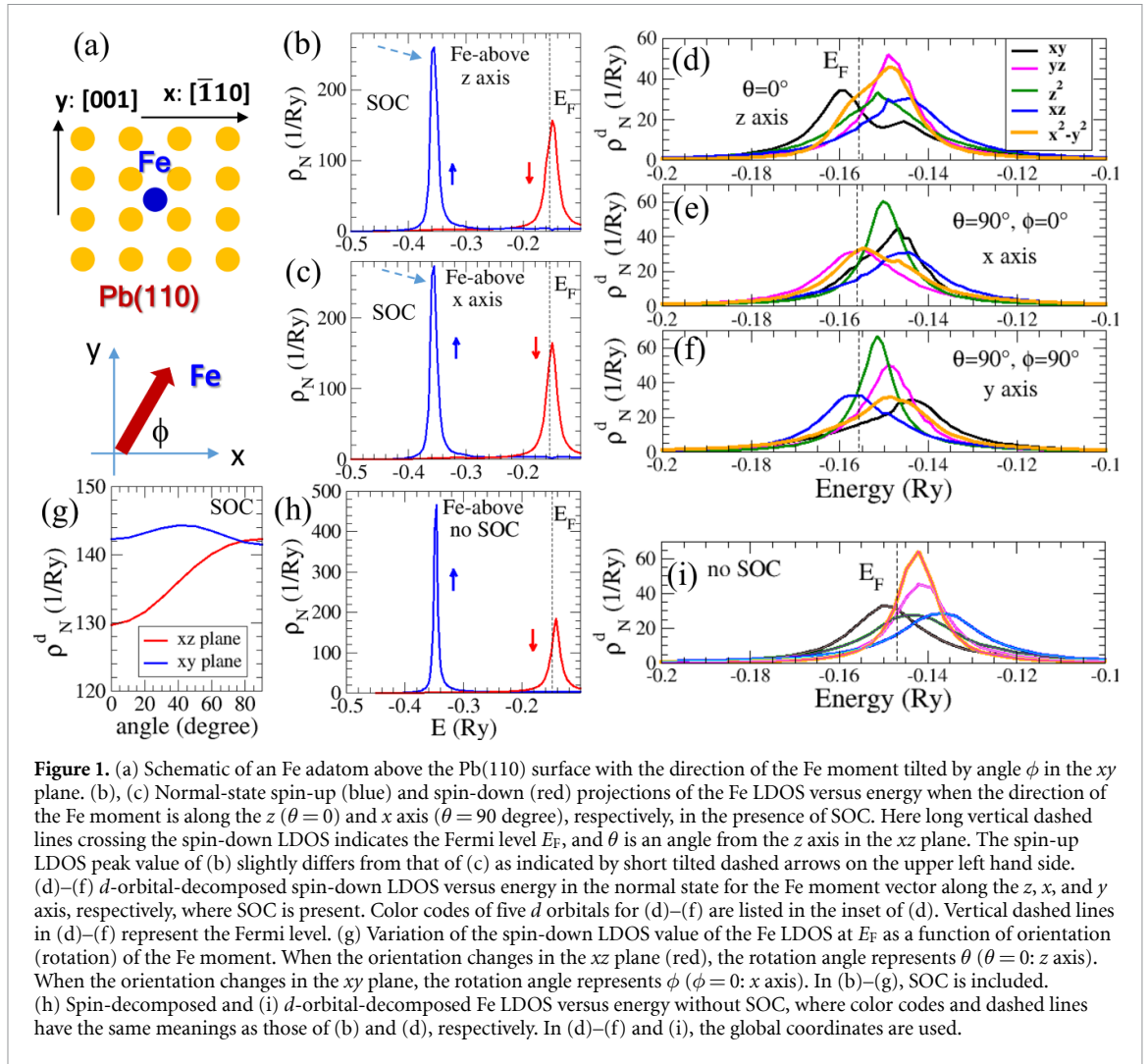
Figure 1. (a) Schematic of an Fe adatom above the Pb(110) surface with the direction of the Fe moment tilted by angle ϕ in the xy plane. (b), (c) Normal-state spin-up (blue) and spin-down (red) projections of the Fe LDOS versus energy when the direction of the Fe moment is along the z ($\theta = 0$) and x axis ($\theta = 90$ degree), respectively, in the presence of SOC. Here long vertical dashed lines crossing the spin-down LDOS indicates the Fermi level E_F, and θ is an angle from the z axis in the xz plane. The spin-up LDOS peak value of (b) slightly differs from that of (c) as indicated by short tilted dashed arrows on the upper left hand side. (d)–(f) d-orbital-decomposed spin-down LDOS versus energy in the normal state for the Fe moment vector along the z, x, and y axis, respectively, where SOC is present. Color codes of five d orbitals for (d)–(f) are listed in the inset of (d). Vertical dashed lines in (d)–(f) represent the Fermi level. (g) Variation of the spin-down LDOS value of the Fe LDOS at E_F as a function of orientation (rotation) of the Fe moment. When the orientation changes in the xz plane (red), the rotation angle represents θ ($\theta = 0$: z axis). When the orientation changes in the xy plane, the rotation angle represents ϕ ($\phi = 0$: x axis). In (b)–(g), SOC is included. (h) Spin-decomposed and (i) d-orbital-decomposed Fe LDOS versus energy without SOC, where color codes and dashed lines have the same meanings as those of (b) and (d), respectively. In (d)–(f) and (i), the global coordinates are used.

Table 1. Normal-state spin and orbital moments of the transition-metal (TM) adatoms and a nearest-neighboring Pb atom, magnetic exchange energy, and existence of zero-energy state (ZES) for the rotations of the moment vectors. In the Fe and Co cases, two different vertical positions of the Fe or Co adatom are considered such as above the Pb surface (TM/Pb(110)) and at the Pb surface (TM-surface/Pb). The TM spin and orbital moments are computed when the TM magnetic moment points along the direction indicated in the parenthesis such as x, y, and z. The magnetic exchange energy is estimated from the spin-down LDOS peak to the spin-up LDOS peak in the normal state. The number next to ZES indicates the number of ZESs with the rotation of the TM moment vectors.

	Fe/Pb(110)	Fe-surface/Pb	Co/Pb(110)	Co-surface/Pb	Mn/Pb(110)
TM spin moment (z)	3.518 μ_B	3.464 μ_B	2.183 μ_B	2.115 μ_B	4.812 μ_B
TM orbital moment (z)	0.906 μ_B	0.665 μ_B	1.215 μ_B	0.857 μ_B	0.027 μ_B
TM spin moment (x)	3.518 μ_B	3.464 μ_B	2.180 μ_B	2.116 μ_B	4.810 μ_B
TM orbital moment (x)	0.780 μ_B	0.601 μ_B	1.176 μ_B	0.948 μ_B	0.078 μ_B
TM spin moment (y)	3.518 μ_B	3.462 μ_B	2.176 μ_B	2.116 μ_B	4.808 μ_B
TM orbital moment (y)	0.743 μ_B	0.585 μ_B	1.142 μ_B	1.001 μ_B	0.113 μ_B
Pb spin moment (z)	0.026 μ_B	0.023 μ_B	0.017 μ_B	0.012 μ_B	0.024 μ_B
Pb orbital moment (z)	0.006 μ_B	0.002 μ_B	0.004 μ_B	0.001 μ_B	0.002 μ_B
TM Exchange energy (z)	0.212 Ry	0.208 Ry	0.134 Ry	0.128 Ry	0.275 Ry
xz-plane rotation	ZES (1)	ZES (1)	ZES (2)	ZES (1)	ZES (0)
xy-plane rotation	ZES (1)	ZES (many)	ZES (0)	ZES (1)	ZES (0)

z axis in the xz plane. Due to twofold rotation symmetry around the z axis and time-reversal symmetry, a quarter of the xz plane suffices to study the effect of moment rotation. The Fe spin-down LDOS at the Fermi level noticeably increases as θ increases (figure 1(g)) with a small change in the spin-up LDOS peak value (figures 1(b) and (c)). The orbital moment decreases to 0.780 μ_B when the moment vector points along the x axis, although the spin moment is not affected (see table 1). Since the amount of charge transfer from the Pb substrate to the Fe adatom does *not* change with the moment orientation for a given vertical distance of the adatom, both the LDOS changes at the Fermi level and the sizeable decrease in the orbital moment imply

remarkable changes in the hybridization with the Pb substrate as a function of the moment orientation. This scenario seems to be supported by a significant influence of the moment orientation on orbital-decomposed spin-down LDOS (figure 1(e) vs (d)). Now we discuss the moment rotation in the xy plane by angle ϕ from the x axis. The C_{2v} point-group symmetry dictates that a quarter of the xy plane suffices to examine the effect of moment rotation. The spin-down LDOS at the Fermi level is subtly modified as a function of rotation angle. The orbital moment slightly further decreases to 0.743 μ_B when the moment vector points along the y axis, without any changes in the spin moment. Orbital-decomposed spin-down LDOS is more noticeably influenced by the Fe moment direction (figure 1(f) vs (d)).

When SOC is turned off in both the Fe adatom and the Pb substrate, the Fermi level slightly increases by 8.12 mRy and the Fe spin magnetic moment is slightly lowered by 0.021 μ_B compared to the SOC-included case. The spin-up Fe LDOS has a narrower linewidth than in the SOC-included case, and it is again well separated from the spin-down Fe LDOS (figure 1(h)). Although the Fermi level is shifted upwards, the spin-down LDOS at the Fermi level is almost the same as in the SOC-included case. Comparing figure 1(i) to figures 1(d)–(f), we find that there are enough differences between the orbital-decomposed LDOS values with and without SOC at the Fermi level, which suggests quite different Shiba states as discussed in sections 3.2 and 3.3.

3.2. Shiba states without SOC
Let us first discuss our calculated LDOS of the Fe impurity in the SC state without SOC. The total Fe LDOS, ρ^{e+h}, reveal five symmetric pairs of peaks, i.e. Shiba states, at energy $E/\Delta = \pm0.22, \pm0.41, \pm0.69, \pm0.77$, and ±0.94 relative to E_F (zero energy), as shown in figure 2(a). The Shiba states at $\pm0.22\Delta$ and $\pm0.41\Delta$ originate from d_{xy} and d_{z^2} orbitals, respectively, while the Shiba states at $\pm0.69\Delta$ and $\pm0.77\Delta$ arise from $\{d_{xz}, d_{yz}\}$ and $d_{x^2-y^2}$ orbitals, respectively. For the Shiba states at $\pm0.69\Delta$, the contributions of d_{xz} and d_{yz} orbitals are too close to be resolved within the numerical accuracy. The Shiba states at $\pm0.94\Delta$ have very small amplitudes and they originate mainly from s orbital. Therefore, without SOC, each Shiba state is well characterized by a single orbital. The fact that the Shiba states of s-orbital character appear near the SC gap edges is consistent with a very small s-orbital LDOS at the Fermi level in the normal state leading to a very weak exchange coupling to the conduction electron spins. The normal-state LDOS values at the Fermi level are somewhat reflected in the ordering of the Shiba states, which agrees with the prediction by Shiba [2]. For example, in the normal state, at the Fermi level, the LDOS of d_{xy} orbital is larger than that of d_{z^2} orbital which is larger than the LDOS of d_{xz} orbital. In the SC state, the Shiba states of d_{xy} orbital appear closest to the zero energy and the next two Shiba states closer to the zero energy are d_{z^2} and d_{xz}/d_{yz} orbitals.

The electron and hole components of the LDOS are shown in figures 2(b) and (c), respectively, and they are further decomposed into spin-down and spin-up projections in figures 2(d)–(g). The Shiba state of d_{xy} character at -0.22Δ consists of a large spin-down *electron* component and a very small spin-up hole component. However, the other three Shiba states of d-orbital character at -0.41, -0.69, and -0.77Δ comprise large spin-down *hole* components and very small spin-up electron components. The characteristics of the Shiba states at the corresponding positive energies are dictated by particle-hole symmetry. Without SOC, a given Shiba state at a negative or positive energy has predominantly either a spin-down electron or a spin-down hole component (figures 2(d)–(g)) rather than having comparable spin-down electron and spin-down hole components. As shown later, that is not the case when SOC is turned on.

3.3. Shiba states with SOC for moment direction along the z axis
Now we turn on SOC in the Fe adatom and the SC substrate when the moment vector is oriented along the z axis. Figure 2(h) shows a total Fe LDOS in the SC state. For convenience, five symmetric pairs of Shiba states are denoted as $\overline{1}$–$\overline{5}$. The electron components at negative energies are labeled as **1**–**5**, while those at positive energies are labeled as **1′**–**5′** (figure 2(i)). Similarly, the hole components are denoted following particle-hole symmetry (figure 2(j)). We find that the energies of the Shiba states are distinct from those without SOC, except for pair $\overline{1}$. Comparing figure 2(a) to figure (h), we observe that with SOC, the four pairs $\overline{2}$–$\overline{5}$ are shifted toward the SC gap edges and multiple orbitals comparably contribute to each of these Shiba states, in contrast to the SOC-free case. Interestingly, two pairs $\overline{3}$ and $\overline{5}$ have comparable spin-down electron and spin-down hole components at negative or positive energies, which is not the case for the Shiba states without SOC.

The above features are due to large mixing between orbital and spin degrees of freedom in the presence of strong SOC. In this case, it may be more convenient to analyze characters of the Shiba states using the total angular momentum, J, and its projection onto the z axis, m_J (or more specifically $|l, s = \frac{1}{2}; J, m_J\rangle$, where l and s are the orbital and spin angular momenta). Table 2 summarizes dominant $|l, \frac{1}{2}; J, m_J\rangle$ contributions to the electron and hole components of each Shiba state. Pair $\overline{1}$ arises from $|0, \frac{1}{2}; \frac{1}{2}, \pm\frac{1}{2}\rangle$ and so it is not affected by SOC. Pair $\overline{2}$ originates mainly from $|2, \frac{1}{2}; \frac{5}{2}, -\frac{5}{2}\rangle$, which is equivalent to $|m_l = -2, m_s = -\frac{1}{2}\rangle$,
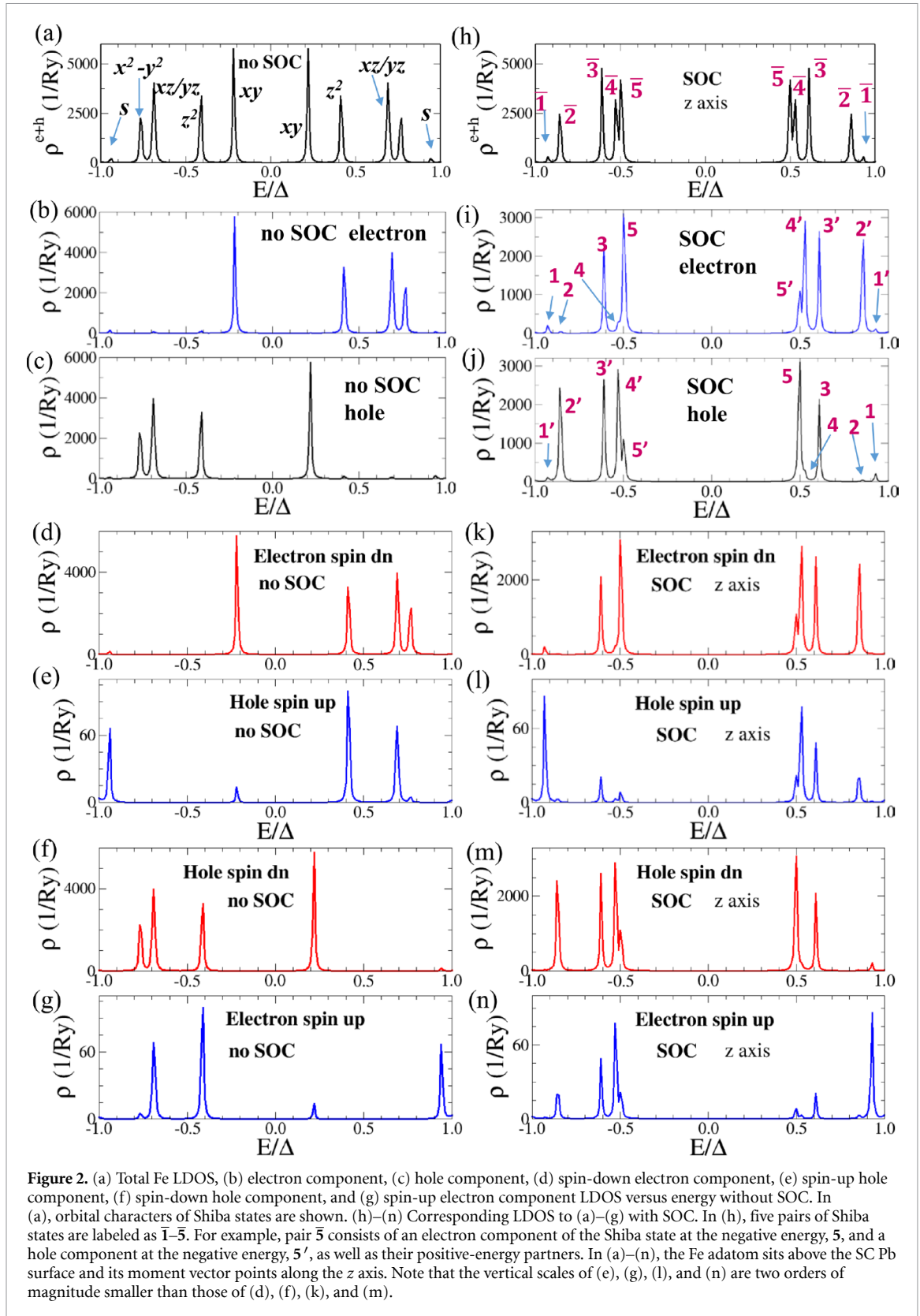
Figure 2. (a) Total Fe LDOS, (b) electron component, (c) hole component, (d) spin-down electron component, (e) spin-up hole component, (f) spin-down hole component, and (g) spin-up electron component LDOS versus energy without SOC. In (a), orbital characters of Shiba states are shown. (h)–(n) Corresponding LDOS to (a)–(g) with SOC. In (h), five pairs of Shiba states are labeled as $\bar{1}$–$\bar{5}$. For example, pair $\bar{5}$ consists of an electron component of the Shiba state at the negative energy, **5**, and a hole component at the negative energy, **5′**, as well as their positive-energy partners. In (a)–(n), the Fe adatom sits above the SC Pb surface and its moment vector points along the *z* axis. Note that the vertical scales of (e), (g), (l), and (n) are two orders of magnitude smaller than those of (d), (f), (k), and (m).

where m_l and m_s are projections of orbital and spin angular momenta along the *z* axis. Since only one spin channel is dominant, for this pair SOC-induced spin mixing is highly suppressed. The fact that only one of the states like 2′ has a large amplitude rather than both states (**2**, **2′**) having substantial amplitudes, is similar to the SOC-free case. For pair $\bar{3}$, both $|2, \frac{1}{2}; \frac{3}{2}, +\frac{3}{2}\rangle$ and $|2, \frac{1}{2}; \frac{5}{2}, +\frac{3}{2}\rangle$ significantly contribute to state **3**, while $|2, \frac{1}{2}; \frac{5}{2}, +\frac{1}{2}\rangle$ and $|2, \frac{1}{2}; \frac{3}{2}, +\frac{1}{2}\rangle$ predominantly contribute to state 3′. Using the Clebsch-Gordon coefficients, state **3** can be rewritten as $\sqrt{\frac{1}{5}}(|m_l = 1, m_s = +\frac{1}{2}\rangle - 2|m_l = 2, m_s = -\frac{1}{2}\rangle)$ and

Table 2. Characteristics of Shiba states from the single Fe adatom in the presence of SOC when the Fe magnetic moment vector points along the *z* axis. The electron components of the negative-energy (positive-energy) Shiba states are labeled as **1–5** (**1′–5′**). The hole components of the Shiba states are labeled by applying particle-hole symmetry to the electron components. Bold-faced electron energies (*e*-energy) and hole energies (*h*-energy) in the third and fourth columns from the left indicate negative energies of the electron and hole components. The degree of SOC-induced spin mixing is indicated at the rightmost column. Here *l* is the orbital angular momentum.

Pair	State	e-energy (Δ)	h-energy (Δ)	Dominant contributions	SOC-induced spin mixing
$\bar{1}$	**1**	**−0.93**	+0.93	$l=0: J=\frac{1}{2}, m_J=-\frac{1}{2}$	Suppressed
	1′	+0.93	**−0.93**	$l=0: J=\frac{1}{2}, m_J=+\frac{1}{2}$	
$\bar{2}$	**2**	**−0.86**	+0.86	$l=1: J=\frac{3}{2}, m_J=+\frac{3}{2}$	Suppressed
	2′	+0.86	**−0.86**	$l=2: J=\frac{5}{2}, m_J=-\frac{5}{2}$	
$\bar{3}$	**3**	**−0.61**	+0.61	$l=2: J=\frac{3}{2}, m_J=+\frac{3}{2}; J=\frac{5}{2}, m_J=+\frac{3}{2}$	Strong
	3′	+0.61	**−0.61**	$l=2: J=\frac{5}{2}, m_J=+\frac{1}{2}; J=\frac{3}{2}, m_J=+\frac{1}{2}$	
$\bar{4}$	**4**	**−0.53**	+0.53	$l=0: J=\frac{1}{2}, m_J=+\frac{1}{2},$	Weak
				$l=2: J=\frac{5}{2}, m_J=+\frac{1}{2}; J=\frac{3}{2}, m_J=+\frac{3}{2}$	
	4′	+0.53	**−0.53**	$l=2: J=\frac{5}{2}, m_J=-\frac{1}{2}; J=\frac{3}{2}, m_J=-\frac{1}{2}$	
$\bar{5}$	**5**	**−0.50**	+0.50	$l=2: J=\frac{3}{2}, m_J=+\frac{3}{2}; J=\frac{5}{2}, m_J=+\frac{3}{2}$	Strong
	5′	+0.50	**−0.50**	$l=2: J=\frac{5}{2}, m_J=+\frac{1}{2}; J=\frac{3}{2}, m_J=+\frac{1}{2}$	

Figure 3. LDOS from five neighboring Pb atoms closest to the Fe adatom above the Pb surface: (a) total LDOS, (b) electron component, and (c) hole component when the Fe magnetic moment vector is oriented along the *z* axis, in the presence of SOC.
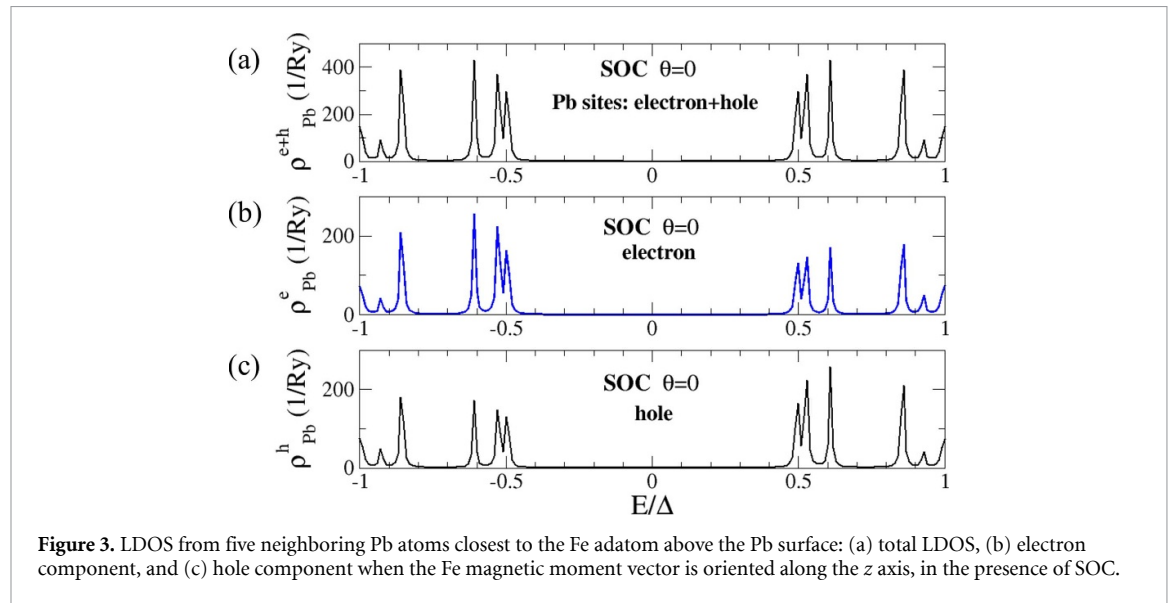
$\sqrt{\frac{1}{5}}(2|m_l=1, m_s=+\frac{1}{2}\rangle + |m_l=2, m_s=-\frac{1}{2}\rangle)$. Similarly, state 3′ can be also rewritten as $\sqrt{\frac{3}{5}}|m_l=0, m_s=+\frac{1}{2}\rangle + \sqrt{\frac{2}{5}}|m_l=1, m_s=-\frac{1}{2}\rangle$ and $\sqrt{\frac{2}{5}}|m_l=0, m_s=+\frac{1}{2}\rangle - \sqrt{\frac{3}{5}}|m_l=1, m_s=-\frac{1}{2}\rangle$. Therefore, both states **3** and 3′ have two spin channels with large amplitudes, and so strong SOC-induced spin mixing is plausible. As a result, the amplitudes of both states (**3**, 3′) are large. Similarly, for pair $\bar{5}$, strong spin-mixing induced by SOC is expected. For pair $\bar{4}$, somewhat more complex $|l, \frac{1}{2}; J, m_J\rangle$ contributions are found (see table 2). The ratio between the amplitude of state **4** and that of state 4′ is small, which indicates weak spin mixing induced by SOC.

3.4. Resonance states from neighboring Pb atoms

When the Fe adatom is located above the Pb surface as discussed earlier, there are five neighboring Pb atoms closest to the Fe adatom and equally separated from the adatom, i.e. four Pb atoms at the topmost Pb layer and one Pb atom below the Fe adatom in the subsurface Pb layer. Considering the orientation of the Fe moment along the *z* axis, we compute the LDOS of these five Pb atoms in the SC state. Some amplitudes at the SC band gap edges must be continued to the continuum DOS outside the SC gap. Firstly, the energies of these resonance states (figure 3(a)) are the same as those of the Shiba states discussed in section 3.3, although their amplitudes are much more reduced than those of the Shiba states. A similar result was obtained for resonances of neighboring boron atoms when a Mn impurity was placed above the surface of MgB$_2$ [42]. Secondly, at either positive or negative energies of all resonance states, both electron and hole components
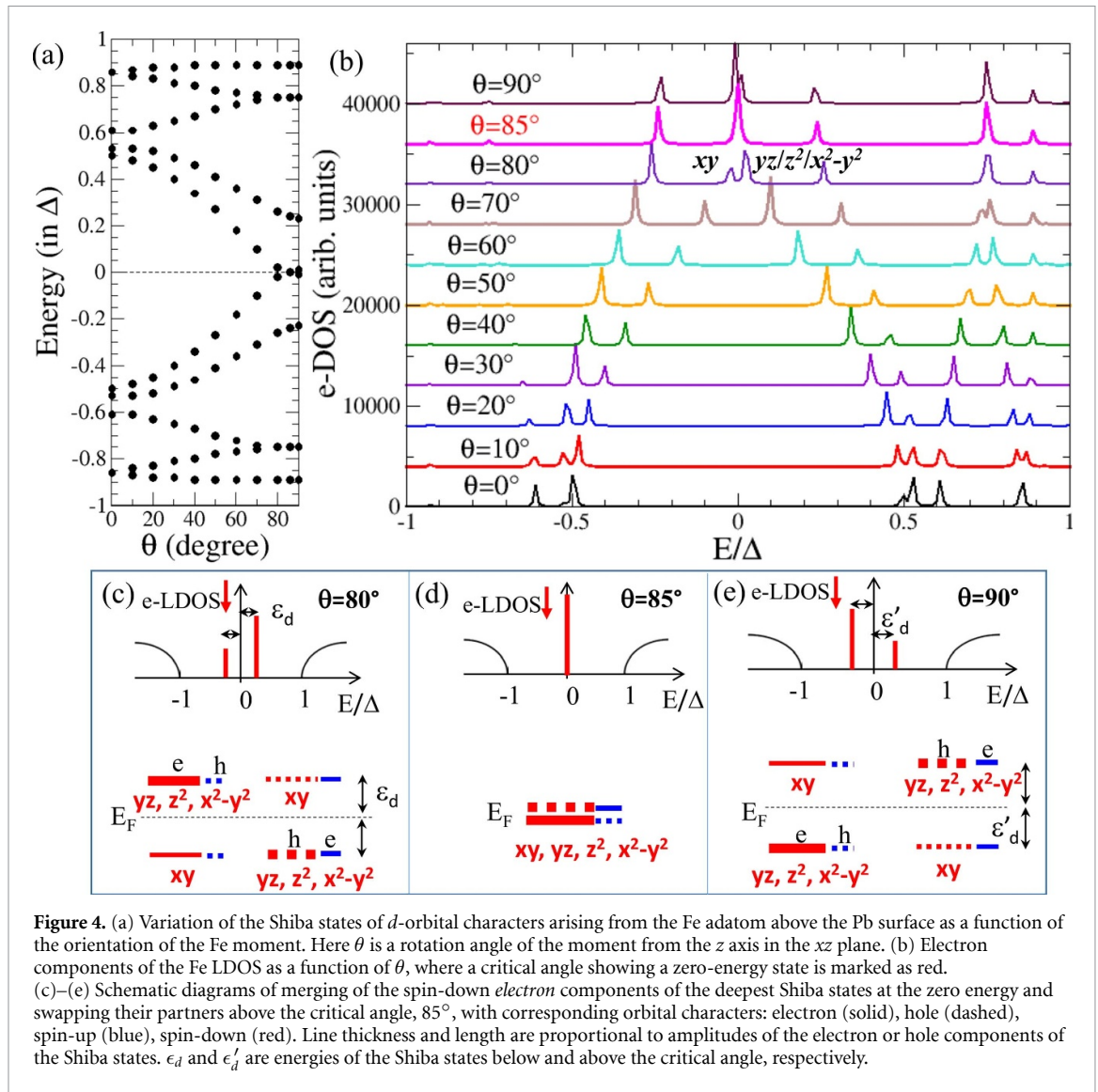
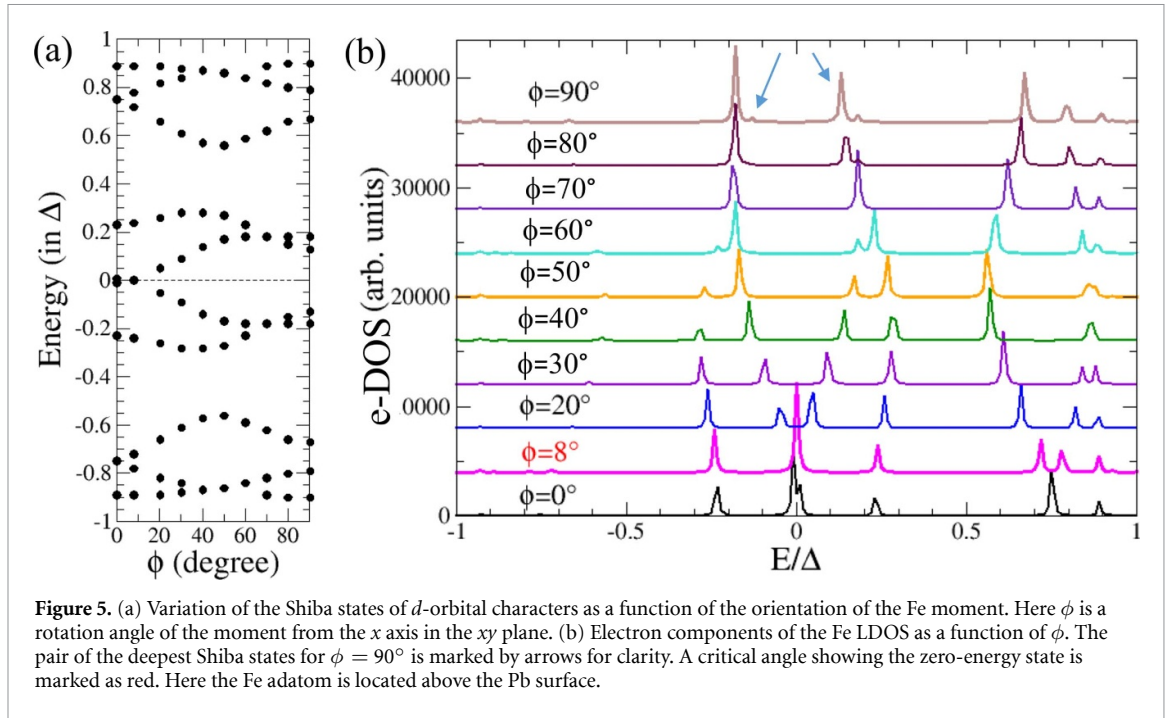**Figure 4.** (a) Variation of the Shiba states of *d*-orbital characters arising from the Fe adatom above the Pb surface as a function of the orientation of the Fe moment. Here θ is a rotation angle of the moment from the *z* axis in the *xz* plane. (b) Electron components of the Fe LDOS as a function of θ, where a critical angle showing a zero-energy state is marked as red. (c)–(e) Schematic diagrams of merging of the spin-down *electron* components of the deepest Shiba states at the zero energy and swapping their partners above the critical angle, 85°, with corresponding orbital characters: electron (solid), hole (dashed), spin-up (blue), spin-down (red). Line thickness and length are proportional to amplitudes of the electron or hole components of the Shiba states. ϵ_d and ϵ'_d are energies of the Shiba states below and above the critical angle, respectively.

contribute almost equally (figures 3(b) and (c)), in contrast to the Shiba states. The two features of the resonance states are due to the small induced magnetic moments in the neighboring Pb atoms by the Fe adatom.

3.5. Shiba states as a function of Fe moment direction

In the presence of SOC, since the orientation of the Fe moment significantly affects the orbital moment and the normal-state LDOS at the Fermi level, apparent changes are expected in energies and characters of the Shiba states. Figure 4(a) shows how the energies of the Shiba states are varied as a function of θ, where states **1** and 1′ are not included since they have mainly *s*-orbital character. As the Fe moment is rotated from the *z* axis, three interesting features are observed: (i) the deepest Shiba states are noticeably shifted toward the Fermi level (i.e. the zero energy); (ii) there is a zero-energy peak in the LDOS around $\theta = 85°$; (iii) pair $\overline{\textbf{2}}$ at $\pm 0.86\Delta$ for $\theta = 0$ splits into two pairs and one of them is merged into another pair. The first feature indicates an increase of effective exchange coupling between the Fe magnetic moment and the conduction electron spins as θ increases. This may be attributed to both the noticeable increase in the normal-state LDOS at the Fermi level with θ (figure 1(g)) and the fact that the Pb substrate has strong Rashba SOC which gives in-plane spin texture. In order to have a better understanding of the zero-energy peak, we compute the electron component of the LDOS as a function of θ (see figure 4(b)). At $\theta = 0$ the pair of the deepest Shiba states includes a negative-energy electron component with a large amplitude and a positive-energy electron component with a small amplitude. As θ increases, the latter becomes to pick up a larger amplitude than the former. Around $\theta = 85°$ the negative-energy electron component of the pair merges with its positive-energy electron component, and then the two components are exchanged for larger θ values ($85° < \theta \leqslant 90°$). This

Figure 5. (a) Variation of the Shiba states of *d*-orbital characters as a function of the orientation of the Fe moment. Here ϕ is a rotation angle of the moment from the *x* axis in the *xy* plane. (b) Electron components of the Fe LDOS as a function of ϕ. The pair of the deepest Shiba states for $\phi = 90°$ is marked by arrows for clarity. A critical angle showing the zero-energy state is marked as red. Here the Fe adatom is located above the Pb surface.

process is schematically shown in figures 4(c)–(e). An analysis of the orbitals contributed to the deepest Shiba states confirms the exchange of the two components.

Figure 5(a) shows how the energies of the Shiba states are varied as a function of ϕ. Overall, the energies of the Shiba states do not change as dramatically as those for the *xz*-plane rotation, although merging and splitting of Shiba states appear. This feature is consistent with the subtle changes of the normal-state LDOS at the Fermi level as a function of ϕ (figure 1(g)). Again we find a zero-energy peak in the LDOS around $\phi = 8°$. Similarly to the case of the *xz* rotation, we compute the electron components of the Shiba states as a function of ϕ (figure 5(b)). From an analysis of them, we find that when the magnetic moment points along the *y* axis, the electron component of the deepest Shiba states at the negative energy has a negligible amplitude, while the corresponding component at the positive energy has a large amplitude. As discussed earlier in section 3.3, this is a signature of strong suppression of spin-mixing. Note that when the moment points along the *z* or *x* axis, such suppression occurs for the Shiba states closer to the SC gap edges rather than near the zero energy.

3.6. Effect of additional non-magnetic adatom on Shiba states

In section 3.5 we have shown that the zero-energy peaks appear in the LDOS at some critical directions of the Fe moment vector. It would be interesting to study if the zero-energy peak remains robust over a small non-magnetic impurity close to the Fe adatom. To this end, we consider a case that a foreign non-magnetic adatom is present right next to the Fe adatom on the Pb substrate. A type of the non-magnetic adatom may not be that important for this study. We simulate a sulfur (S) atom located at the nearest neighboring site of the Fe adatom along the *x* axis on Pb(110). Both the Fe and S adatoms are at the same vertical distance from the Pb surface. When the Fe moment vector is rotated, the S moment vector is also rotated almost antiparallel to the Fe moment. In the normal state, the spin and orbital magnetic moments of the S adatom as well as the changes of the Fe moments are only an order of 0.01% of the spin and orbital moments of the Fe adatom in the S-free case, independently of the moment direction. Therefore, we expect a minimum effect of the S adatom on the Shiba states.

We calculate the Fe LDOS of this system in the SC state as a function of rotation angle θ (figure 6). This LDOS can be compared to the Fe LDOS in the S-free case (section 3.5), since the contribution of the S LDOS is negligible. For an analysis, we compare the electron components of the Shiba states in this case to those in section 3.5 (figure 6 vs 4(b)). As expected, overall, the energies of the Shiba states barely change for most θ values. However, a zero-energy peak is now absent in the Fe LDOS at all considered angles. In order to show that this is not due to numerical accuracy, we focus on the electron components of the deepest Shiba states sufficiently close to the zero energy, i.e. for $80° \leqslant \theta \leqslant 90°$. For a zero-energy peak to appear in this range of θ, the amplitudes and the orbital character of the electron components at the negative and positive energies must be reversed relative to a critical angle, as illustrated in figures 4(c)–(e). Such a feature is not observed at
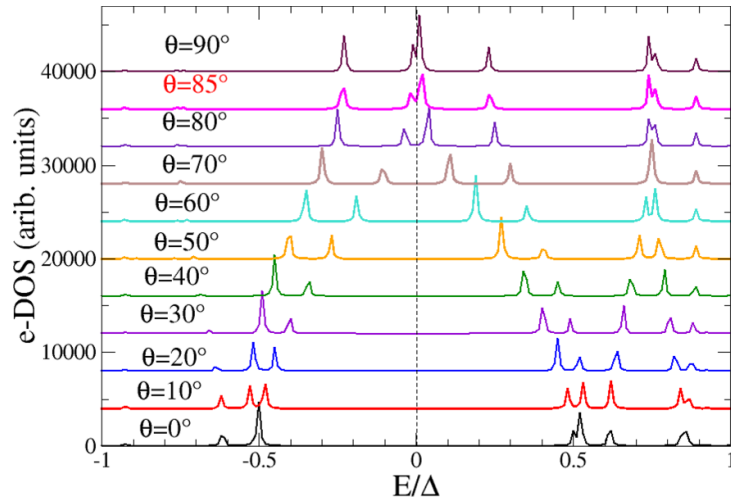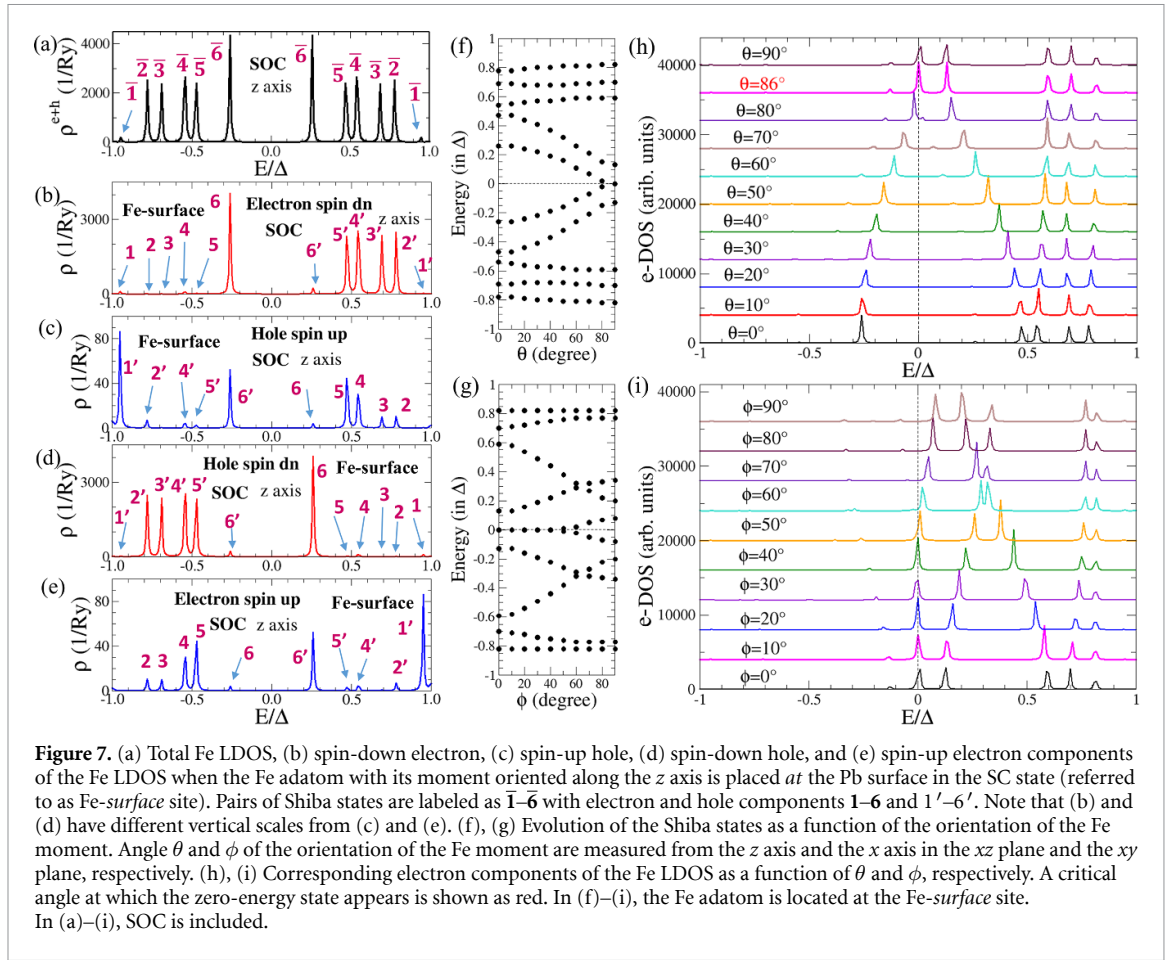
Figure 6. Electron components of the Fe LDOS as a function of the orientation of the Fe–S moment when a non-magnetic S adatom is present right next to the Fe adatom with the same vertical distance above the Pb surface. Here θ is a rotation angle of the moment from the *z* axis in the *xz* plane.

any θ values in the range (figure 6). This suggests that the tiny change made by a non-magnetic atom can be enough for avoiding the Fermi level crossing, and consequently for the zero-energy state to disappear.

3.7. Effect of Fe vertical distance on Shiba states

Due to different atomic sizes of Fe and Pb, there is a possibility that the Fe adatom may be located somewhat below the hollow site which we have so far considered. In order to study an effect of Fe vertical distance from the surface, we consider a Fe adatom located at the Pb surface layer, i.e. replacing one of the Pb surface atoms by Fe, which is, henceforth, referred to as Fe-*surface* site. The position of the Fe adatom discussed in sections 3.1–3.6 is referred to as Fe-*above* site. In the normal state, when the Fe moment is oriented along the *z* axis, the spin-up and spin-down Fe LDOS in the Fe-*surface* case are as well-separated as those in the Fe-*above* case (see section 3.1). The spin-down LDOS at the Fermi level in the Fe-*surface* case is about 88% of that in the Fe-*above* case, which is attributed to slightly more broadened LDOS in the former. The spin and orbital moments of the Fe adatom are now 3.464 and 0.665 μ_B. The orbital moment decreases by 0.341 μ_B, while the spin moment decreases only by 0.054 μ_B, compared to the moments for the Fe-*above* case. The more broadened LDOS and moment changes can be understood from an increase in the charge transfer from the Pb substrate to the Fe adatom as well as larger hybridization with the Pb substrate than in the Fe-*above* case. When the Fe moment is oriented along the *x* or *y* axis, the orbital moment slightly changes but the spin moment remains almost the same as that for the *z* axis (see table 1). There are also small induced spin and orbital moments on neighboring Pb atoms.

  Now let us discuss the Fe LDOS in the SC state when the Fe moment is oriented along the *z* axis. We identify six pairs of Shiba states at ± 0.95, ± 0.78, ± 0.69, ± 0.54, ± 0.47, and $\pm 0.26\Delta$, which are labeled as $\overline{1}$–$\overline{6}$, respectively, as shown in figure 7(a). Similarly to figures 2(h)–(n) in section 3.3, each pair consists of electron and hole components at positive and negative energies. For example, pair $\overline{5}$ comprises electron and hole components **5** and 5′ at $\pm 0.47\Delta$. The Shiba states in the Fe-*surface* case have some similarities to those in the Fe-*above* case. Pair $\overline{1}$ at $\pm 0.95\Delta$ mainly arises from the *s* orbital, which is similar to pair $\overline{1}$ in figure 2(h) in the Fe-*above* case. In addition, pairs $\overline{1}$, $\overline{3}$, $\overline{5}$, and $\overline{6}$ in the Fe-*surface* case have similar orbitals and $|l, s = \frac{1}{2}; J, m_J\rangle$ characteristics to pairs $\overline{1}$, $\overline{2}$, $\overline{4}$, and $\overline{5}$ in the Fe-*above* case, respectively (figure 7(a) vs 2(h)). The Shiba states in the Fe-*surface* case, however, have several major differences from those in the Fe-*above* case. Some differences are that there is one more pair of Shiba states and that the deepest pair of Shiba states is much closer to the zero energy, compared to the Fe-*above* case. Another noticeable difference is that in the Fe-*surface* case, electron (or hole) components of all the Shiba states do *not* have significant amplitudes at both positive and negative energies (figures 7(b)–(e)). For instance, in the Fe-*surface* case, for pair $\overline{4}$, the electron component of the Shiba states has a large amplitude at the positive energy (4′, $+0.54\Delta$) and a tiny amplitude at the corresponding negative energy (**4**, -0.54Δ). This implies that SOC-induced spin mixing is highly suppressed in the Fe-*surface* case. Note that for pairs $\overline{3}$ and $\overline{5}$ in the Fe-*above* case, the electron (or hole) components of the Shiba states have large or substantial amplitudes at both positive and negative energies (figures 2(h)–(j)), which indicates strong spin mixing induced by SOC .

Figure 7. (a) Total Fe LDOS, (b) spin-down electron, (c) spin-up hole, (d) spin-down hole, and (e) spin-up electron components of the Fe LDOS when the Fe adatom with its moment oriented along the *z* axis is placed *at* the Pb surface in the SC state (referred to as Fe-*surface* site). Pairs of Shiba states are labeled as **$\bar{1}$–$\bar{6}$** with electron and hole components **1–6** and **1′–6′**. Note that (b) and (d) have different vertical scales from (c) and (e). (f), (g) Evolution of the Shiba states as a function of the orientation of the Fe moment. Angle θ and ϕ of the orientation of the Fe moment are measured from the *z* axis and the *x* axis in the *xz* plane and the *xy* plane, respectively. (h), (i) Corresponding electron components of the Fe LDOS as a function of θ and ϕ, respectively. A critical angle at which the zero-energy state appears is shown as red. In (f)–(i), the Fe adatom is located at the Fe-*surface* site. In (a)–(i), SOC is included.

When the orientation of the Fe moment changes from the *z* axis in the *xz* plane, the evolution of the energies of the Shiba states as a function of θ is similar to that in section 3.5 (figure 7(f) vs 4(a)). There is also a zero-energy peak near $\theta = 86°$ below and above which the electron components of the deepest Shiba states at the negative and positive energies are exchanged, as shown in figure 7(h). Regarding the rotation of the Fe moment in the *xy* plane, the energies of the Shiba states varies as a function of ϕ similarly to the Fe-*above* case (figure 7(g) vs 5(a)) for small ϕ values, whereas the angular dependence is modified to great extent for intermediate and large θ values. Interestingly, there is a large window of ϕ where a zero-energy state or nearly-zero-energy state appears (see figure 7(i)).

To sum up, for the Fe-*surface* site, there are larger charge transfer and stronger hybridization with the Pb substrate than the Fe-*above* site, which entails the noticeable reduction in the Fe orbital moment and the deepest Shiba states closer to the zero energy. When the Fe moment vector points along the *z* axis, the characteristics of some Shiba states (i.e. the states closer to the zero energy and states near the SC gap edges) remain very similar for the two Fe vertical distances. The energies of the Shiba states in the whole range of θ and at small ϕ values are *not* very sensitive to the vertical distance of the Fe adatom. A zero-energy state also appears as the orientation of the moment is varied for the Fe-*surface* site.

4. Co adatom on Pb(110)

4.1. Properties of the normal state

When a Co adatom is at the hollow site above the Pb surface, some features of the Co LDOS in the normal state are similar to those of the Fe adatom. Therefore, we discuss mainly differences between the two cases. When the Co moment is oriented along the *z* axis, the spin and orbital moments of the Co adatom are computed to be 2.183 and 1.215 μ_B, respectively. They are much smaller than the nominal values of an isolated Co atom which are 3.0 μ_B for both spin and orbital moments. This deviation is much more significant than that in the Fe case, despite the same vertical distance of the Fe and Co adatoms. Therefore, the Co adatom seems to be much more hybridized with the Pb substrate than the Fe adatom.

Since the Fermi level lies almost at the peak of the spin-down LDOS for the Co adatom, the spin-down LDOS at the Fermi level in the Co case is higher than in the Fe case (figure 8(a) vs 1(b)). Thus the exchange
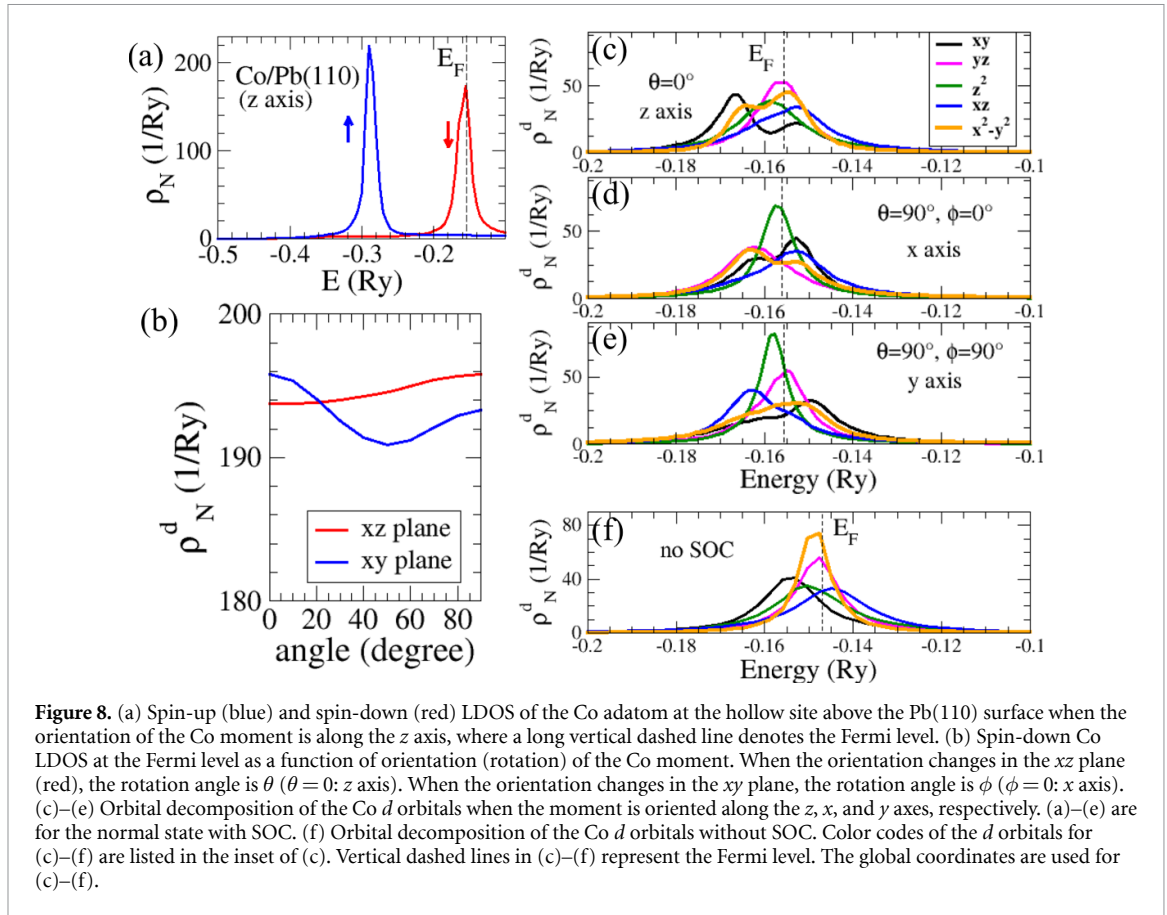
Figure 8. (a) Spin-up (blue) and spin-down (red) LDOS of the Co adatom at the hollow site above the Pb(110) surface when the orientation of the Co moment is along the *z* axis, where a long vertical dashed line denotes the Fermi level. (b) Spin-down Co LDOS at the Fermi level as a function of orientation (rotation) of the Co moment. When the orientation changes in the *xz* plane (red), the rotation angle is θ ($\theta = 0$: *z* axis). When the orientation changes in the *xy* plane, the rotation angle is ϕ ($\phi = 0$: *x* axis). (c)–(e) Orbital decomposition of the Co *d* orbitals when the moment is oriented along the *z*, *x*, and *y* axes, respectively. (a)–(e) are for the normal state with SOC. (f) Orbital decomposition of the Co *d* orbitals without SOC. Color codes of the *d* orbitals for (c)–(f) are listed in the inset of (c). Vertical dashed lines in (c)–(f) represent the Fermi level. The global coordinates are used for (c)–(f).
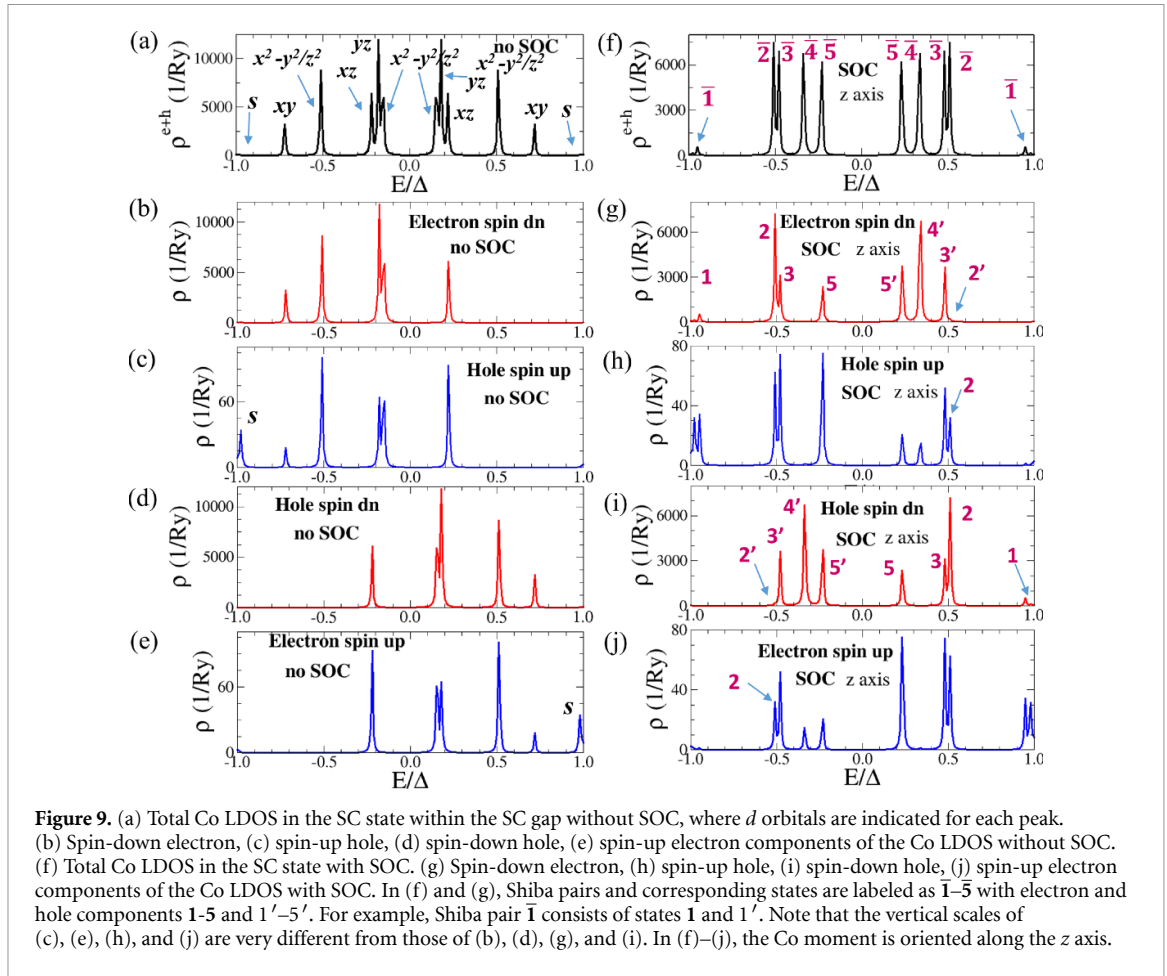
coupling to the conduction electron spins is expected to be stronger than in the Fe case. The peak-to-peak energy difference between the spin-up and spin-down Co LDOS is about 0.078 Ry smaller than that of the Fe LDOS. The Co LDOS shows a somewhat weaker dependence on the moment orientation than the Fe LDOS (figure 8(b) vs 1(g)). The decomposition of the Co *d* orbitals at the Fermi level substantially differs from that of the Fe *d* orbitals with and without SOC (figures 8(c)–(f) vs 1(d)–(f),(i)).

4.2. Shiba states without SOC

In the SC state, without SOC, the total Co LDOS shows six pairs of Shiba states at $E/\Delta = \pm 0.15$, ± 0.18, ± 0.22, ± 0.51, ± 0.72, and ± 0.98, as shown in figure 9(a). They originate from $\{d_{z^2}, d_{x^2-y^2}\}$, d_{yz}, d_{xz}, $\{d_{x^2-y^2}, d_{z^2}\}$, d_{xy}, and *s* orbitals, respectively. The small peaks at $\pm 0.98\Delta$ are marked by arrows in figure 9(a). The energies and characters of the Shiba states qualitatively differ from those of the Fe case, except for the Shiba state of *s* orbital at $\pm 0.98\Delta$. Comparing the Shiba states with the orbital-decomposed normal-state Co LDOS (figure 8(f)), we find that the *d* orbital with the largest LDOS at the Fermi level, $d_{x^2-y^2}$, contributes to the deepest pair of Shiba states and that the *d* orbital with the smallest LDOS at the Fermi level, d_{xy}, contributes to the farthest pair of Shiba states except for the *s*-orbital, within the SC gap. Overall, for each *d* orbital, the order of the Shiba states within the gap is consistent with the normal-state LDOS of each *d* orbital at the Fermi level. This observation suggests that higher normal-state LDOS at the Fermi level can be considered as an indicator of stronger effective exchange coupling to the conduction electron spin. This is consistent with the prediction by Shiba [2]. Similarly to the Fe case, without SOC, for a given negative or positive energy, either an electron or a hole component of the Shiba state is dominant rather than both components (see figures 9(b)–(e)).

4.3. Shiba states with SOC for Co moment along the z axis

When the Co moment vector is oriented along the *z* axis, five pairs of Shiba states appear at $E/\Delta = \pm 0.23$, ± 0.34, ± 0.48, ± 0.51, and ± 0.95, which are respectively labeled as $\bar{5}$, $\bar{4}$, $\bar{3}$, $\bar{2}$, and $\bar{1}$, as shown in figure 9(f). Table 3 shows characters of the pairs of Shiba states using $|l, s = \frac{1}{2}; J, m_J\rangle$ states. Pair $\bar{1}$ at $\pm 0.95\Delta$ has some $|l = 0, s = \frac{1}{2}; J = \frac{1}{2}, m_J = \frac{1}{2}\rangle$ character, which is similar to that in the Fe case. However, all Shiba states of *d*-orbital characters ($|l = 2, s = \frac{1}{2}; J = \frac{5}{2}, m_J\rangle$; $|l = 2, s = \frac{1}{2}; J = \frac{3}{2}, m_J\rangle$) now appear within an energy window of $[-0.51\Delta, +0.51\Delta]$, while all Shiba states of the similar characters are shown outside this energy window in the Fe case. For pairs $\bar{3}$ and $\bar{5}$, two spin channels are present and thus both electron and hole components
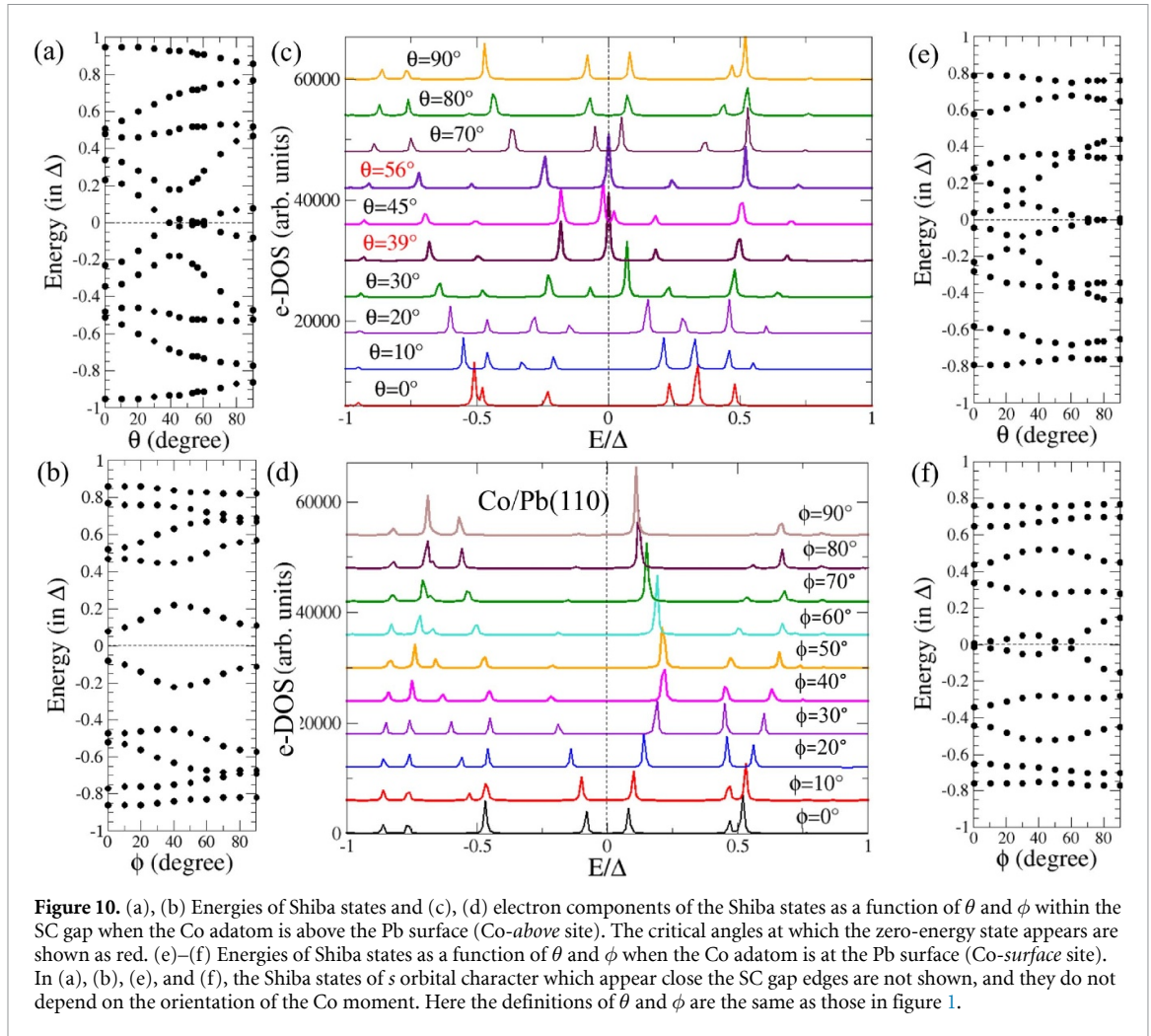
Figure 9. (a) Total Co LDOS in the SC state within the SC gap without SOC, where *d* orbitals are indicated for each peak. (b) Spin-down electron, (c) spin-up hole, (d) spin-down hole, (e) spin-up electron components of the Co LDOS without SOC. (f) Total Co LDOS in the SC state with SOC. (g) Spin-down electron, (h) spin-up hole, (i) spin-down hole, (j) spin-up electron components of the Co LDOS with SOC. In (f) and (g), Shiba pairs and corresponding states are labeled as $\bar{1}$–$\bar{5}$ with electron and hole components 1-5 and 1′–5′. For example, Shiba pair $\bar{1}$ consists of states **1** and 1′. Note that the vertical scales of (c), (e), (h), and (j) are very different from those of (b), (d), (g), and (i). In (f)–(j), the Co moment is oriented along the *z* axis.

Table 3. Characteristics of Shiba states from the single Co adatom in the presence of SOC when the Co magnetic moment points along the *z* axis. The electron components of the negative-energy (positive-energy) Shiba states are labeled as 1–5 (1′–5′) (see figures 9(g) and (j)). The hole components of the Shiba states are labeled by applying particle-hole symmetry to the electron components (see figures 9(h) and (i)). Bold-faced electron energies (*e*-energy) and hole energies (*h*-energy) in the third and fourth columns from the left indicate negative energies of the electron and hole components. The definitions of the symbols are the same as those in table 2.

Pair	State	*e*-energy (Δ)	*h*-energy (Δ)	Dominant contributions	SOC-induced spin mixing
$\bar{1}$	**1**	**−0.95**	+0.95	$l=2: J=\frac{3}{2}, m_J=+\frac{3}{2}$	Suppressed
	1′	+0.95	**−0.95**	$l=0: J=\frac{1}{2}, m_J=+\frac{1}{2}$	
$\bar{2}$	**2**	**−0.51**	+0.51	$l=2: J=\frac{5}{2}, m_J=+\frac{1}{2}; J=\frac{3}{2}, m_J=+\frac{1}{2}$	Weak
	2′	+0.51	**−0.51**	$l=2: J=\frac{5}{2}, m_J=-\frac{3}{2}; J=\frac{3}{2}, m_J=-\frac{1}{2}$	
$\bar{3}$	**3**	**−0.48**	+0.48	$l=2: J=\frac{5}{2}, m_J=-\frac{1}{2}; J=\frac{3}{2}, m_J=-\frac{1}{2}$	Strong
	3′	+0.48	**−0.48**	$l=2: J=\frac{5}{2}, m_J=-\frac{3}{2}; J=\frac{3}{2}, m_J=-\frac{3}{2}$	
$\bar{4}$	**4**	**−0.34**	+0.34	$l=2: J=\frac{5}{2}, m_J=+\frac{5}{2}$	Suppressed
	4′	+0.34	**−0.34**	$l=2: J=\frac{5}{2}, m_J=-\frac{5}{2}$	
$\bar{5}$	**5**	**−0.23**	+0.23	$l=2: J=\frac{5}{2}, m_J=-\frac{1}{2}; J=\frac{3}{2}, m_J=-\frac{1}{2}$	Strong
	5′	+0.23	**−0.23**	$l=2: J=\frac{5}{2}, m_J=-\frac{3}{2}; J=\frac{3}{2}, m_J=-\frac{3}{2}$	

of the Shiba states are comparable (figures 9(g)–(j)). This implies strong spin mixing induced by SOC. On the other hand, for pairs $\bar{1}$ and $\bar{4}$, only single spin channels are dominant and thus such spin mixing is highly suppressed.

4.4. Shiba states for rotation of Co moment

Figures 10(a) and (b) shows how the energies of the Shiba states evolve as functions of rotation angles θ and ϕ for the Co adatom above the Pb surface, when the Co moment vector is rotated in the *xz* and *xy* planes, respectively. An analysis of the electron components of the Shiba states indicates that as θ increases, the deepest Shiba states move closer to the zero energy and they merge at the zero energy around 39°. For

Figure 10. (a), (b) Energies of Shiba states and (c), (d) electron components of the Shiba states as a function of θ and ϕ within the SC gap when the Co adatom is above the Pb surface (Co-*above* site). The critical angles at which the zero-energy state appears are shown as red. (e)–(f) Energies of Shiba states as a function of θ and ϕ when the Co adatom is at the Pb surface (Co-*surface* site). In (a), (b), (e), and (f), the Shiba states of *s* orbital character which appear close the SC gap edges are not shown, and they do not depend on the orientation of the Co moment. Here the definitions of θ and ϕ are the same as those in figure 1.

$\theta > 39°$, the electron component of the deepest Shiba state with a smaller amplitude is exchanged with that with a larger amplitude and the two electron components merge again around 56° (figure 10(c)). However, when the Co moment vector rotates in the *xy* plane, a zero-energy state is not realized (figure 10(d)). The evolution of the Shiba-state energies as functions of θ and ϕ is distinct from that in the Fe case, which may be due to much stronger hybridization of the Co adatom to the Pb substrate.
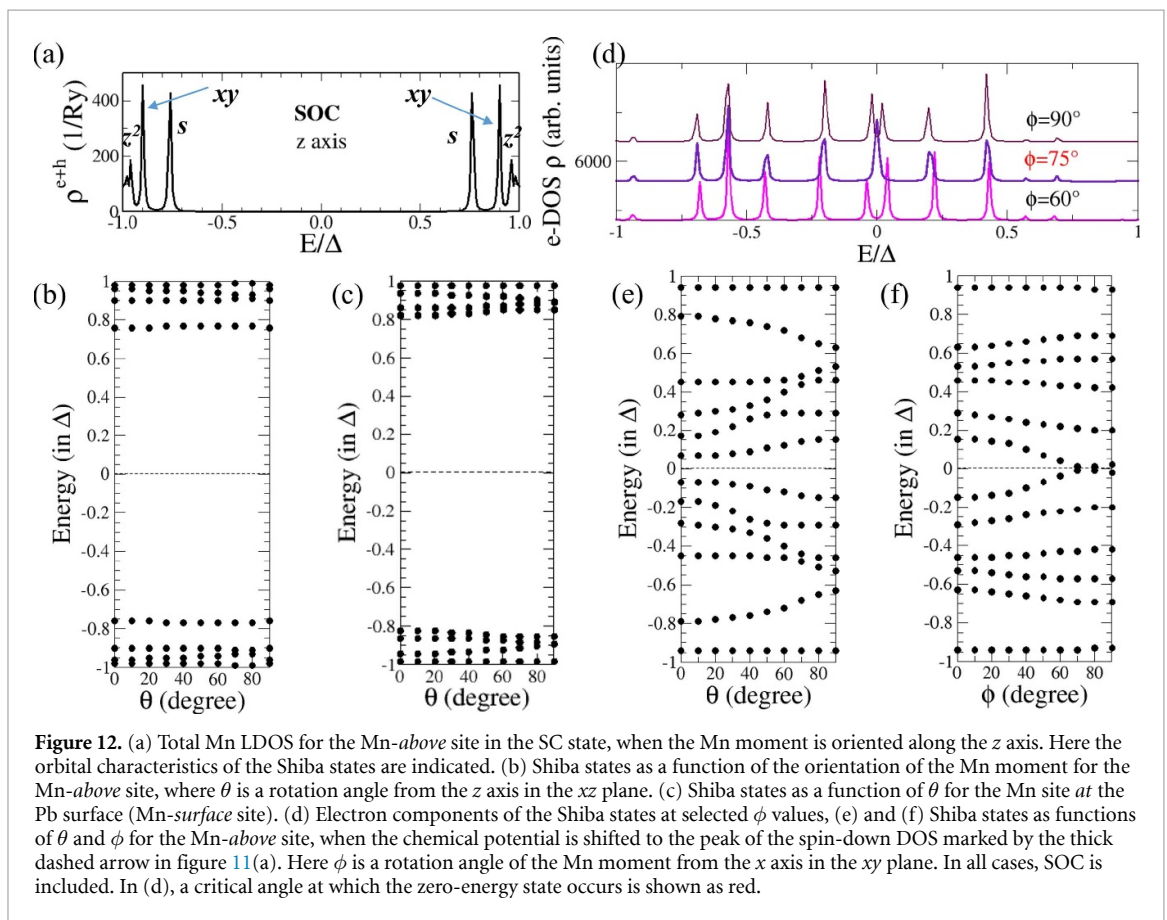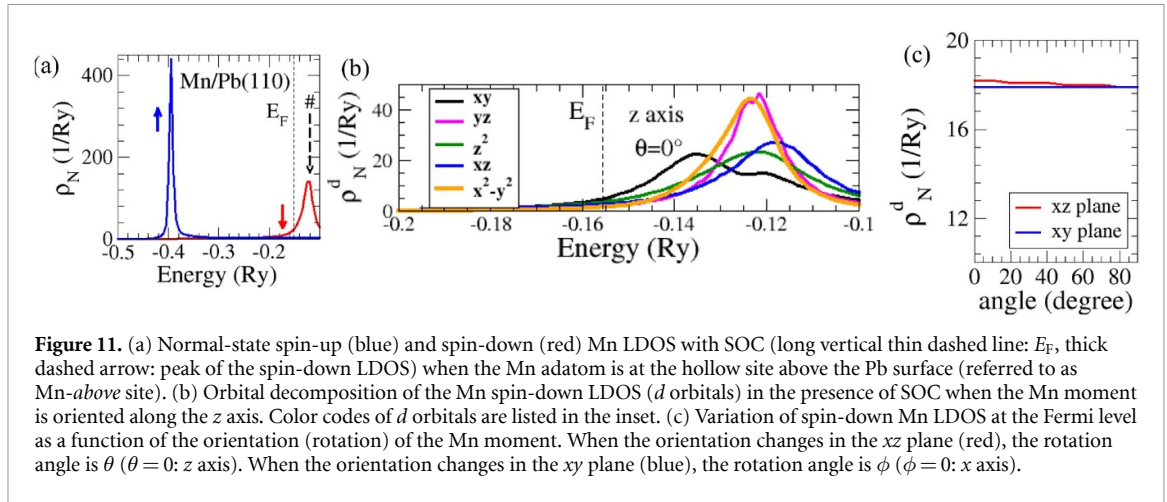
4.5. Effect of different Co vertical distance on Shiba states

Now let us discuss a case that the Co adatom sits in the Pb surface layer (referred to as Co-*surface* site), when the moment is oriented along the *z* axis. Shiba states in this case overall appear deeper in the SC gap than in the case of the Co adatom above the Pb surface (referred to as Co-*above* site), as shown in figure 10(e) vs (a). This result is consistent with the fact that the lower Co vertical distance, the stronger exchange coupling to the conduction electron spins. Figures 10(e) and (f) shows how the energies of the Shiba states evolve as functions of rotation angles θ and ϕ for the Co-*surface* case. For the rotation in the *xz* plane, a zero-energy state now appears around 76°, while for the rotation in the *xy* plane, it occurs around 54°. Note that a zero-energy state is not formed for the rotation in the *xy* plane in the Co-*above* case. The angular dependence of the Shiba states in the Co-*surface* case qualitatively differs from that for the Co-*above* case (section 4.4) except for the outermost two pairs of the Shiba states. This angular dependence in the Co-*surface* case is also distinct from that in the Fe-*surface* case (section 3.7) and that in the Fe-*above* case (section 3.5).

5. Mn adatom on Pb(110)

5.1. Properties of the normal state

When the Mn adatom is at the hollow site above the Pb surface, the spin and orbital moments of the Mn adatom are computed to be 4.812 and 0.027 μ_B, respectively, which are much closer to those of an isolated Mn atom (5.0 and 0.0 μ_B) than those for the Fe or0 Co case (see table 1). Therefore, we expect that hybridization with the Pb substrate is much weaker than that of the Fe or Co adatom. The Mn adatom has

Figure 11. (a) Normal-state spin-up (blue) and spin-down (red) Mn LDOS with SOC (long vertical thin dashed line: E_F, thick dashed arrow: peak of the spin-down LDOS) when the Mn adatom is at the hollow site above the Pb surface (referred to as Mn-*above* site). (b) Orbital decomposition of the Mn spin-down LDOS (d orbitals) in the presence of SOC when the Mn moment is oriented along the z axis. Color codes of d orbitals are listed in the inset. (c) Variation of spin-down Mn LDOS at the Fermi level as a function of the orientation (rotation) of the Mn moment. When the orientation changes in the xz plane (red), the rotation angle is θ ($\theta = 0$: z axis). When the orientation changes in the xy plane (blue), the rotation angle is ϕ ($\phi = 0$: x axis).

Figure 12. (a) Total Mn LDOS for the Mn-*above* site in the SC state, when the Mn moment is oriented along the z axis. Here the orbital characteristics of the Shiba states are indicated. (b) Shiba states as a function of the orientation of the Mn moment for the Mn-*above* site, where θ is a rotation angle from the z axis in the xz plane. (c) Shiba states as a function of θ for the Mn site *at* the Pb surface (Mn-*surface* site). (d) Electron components of the Shiba states at selected ϕ values, (e) and (f) Shiba states as functions of θ and ϕ for the Mn-*above* site, when the chemical potential is shifted to the peak of the spin-down DOS marked by the thick dashed arrow in figure 11(a). Here ϕ is a rotation angle of the Mn moment from the x axis in the xy plane. In all cases, SOC is included. In (d), a critical angle at which the zero-energy state occurs is shown as red.

also well-separated spin-up and spin-down LDOS in the normal state. The peak-to-peak energy difference between the spin-up and spin-down LDOS is about 0.275 Ry, which is significantly larger than that in the Fe or Co case. Since the Fermi level lies at the tail of the Mn spin-down LDOS (figure 11(a)), the spin-down LDOS at the Fermi level is about one order of magnitude lower than the corresponding value in the Fe or Co case. The LDOS at the Fermi level does not depend much on the orientation of the Mn moment (figure 11(c)).

5.2. Shiba states with SOC

In the SC state, for the Mn adatom above the Pb surface, we observe four pairs of Shiba states at $\pm 0.76\Delta$, $\pm 0.91\Delta$, $\pm 0.96\Delta$, and $\pm 0.98\Delta$ (figure 12(a)), when the Mn moment is oriented along the z axis. Compared to the Fe or Co case, all of the Shiba states appear very close to the SC gap edges. This is attributed to a very small exchange coupling to the conduction electron spins, which is consistent with the very small normal-state LDOS at the Fermi level, despite the largest spin moment of the Mn adatom. The Shiba states at

$\pm 0.98\Delta$ arise from large and small contributions of $d_{x^2-y^2}$ and d_{z^2} orbitals, respectively. This is in contrast to the case of Fe and Co adatoms, where the pair of Shiba states closest to the SC gap edges originates from s orbital. The Shiba states at $\pm 0.96\Delta$ and $\pm 0.90\Delta$ have characters of d_{z^2} and d_{xy} orbitals, respectively. The fact that the Shiba states of d_{xy} character appear a bit farther from the SC gap edges than those of d_{z^2} character is consistent with the orbital decomposition of the spin-down LDOS at the Fermi level (figure 11(b)). Interestingly, in the Mn case, the s-orbital contributions to the Shiba states occur *not* too close to the SC gap edges such as at $\pm 0.76\Delta$. All of the Shiba states do not noticeably depend on the orientation of the Mn moment in the xz plane (figure 12(b)) and in xy plane (not shown). Even when the Mn adatom sits in the Pb surface layer, the energies of the Shiba states barely change with the orientation of the Mn moment (figure 12(c)).

In order to show an importance of large normal-state impurity DOS, we calculate the Mn LDOS in the SC state for the Mn adatom above the Pb surface when the chemical potential in the normal state is raised to the peak of the spin-down LDOS marked in figure 11(a). Figures 12(e) and (f) show Shiba states as functions of θ and ϕ in this case. First of all, now for $\theta = 0$, the deepest Shiba states appear very close to the zero energy, i.e. strong exchange coupling to the conduction electrons. Secondly, the calculated Shiba states strongly depend on the orientation of the Mn moment. Thirdly, for the rotation in the xy plane, there is a zero-energy state around $\phi = 75°$ (figure 12(d)), similarly to the Fe or Co case.

6. Comparison to experiments

There are no experimental data on Shiba states arising from single Fe, Co, and Mn adatoms on Pb(110). It was reported in [10] that for single Fe adatoms on Pb(110), there were *no d*-orbital resonances within the SC gap, while Fe dimers on Pb(110) showed several Shiba pairs within the SC gap.
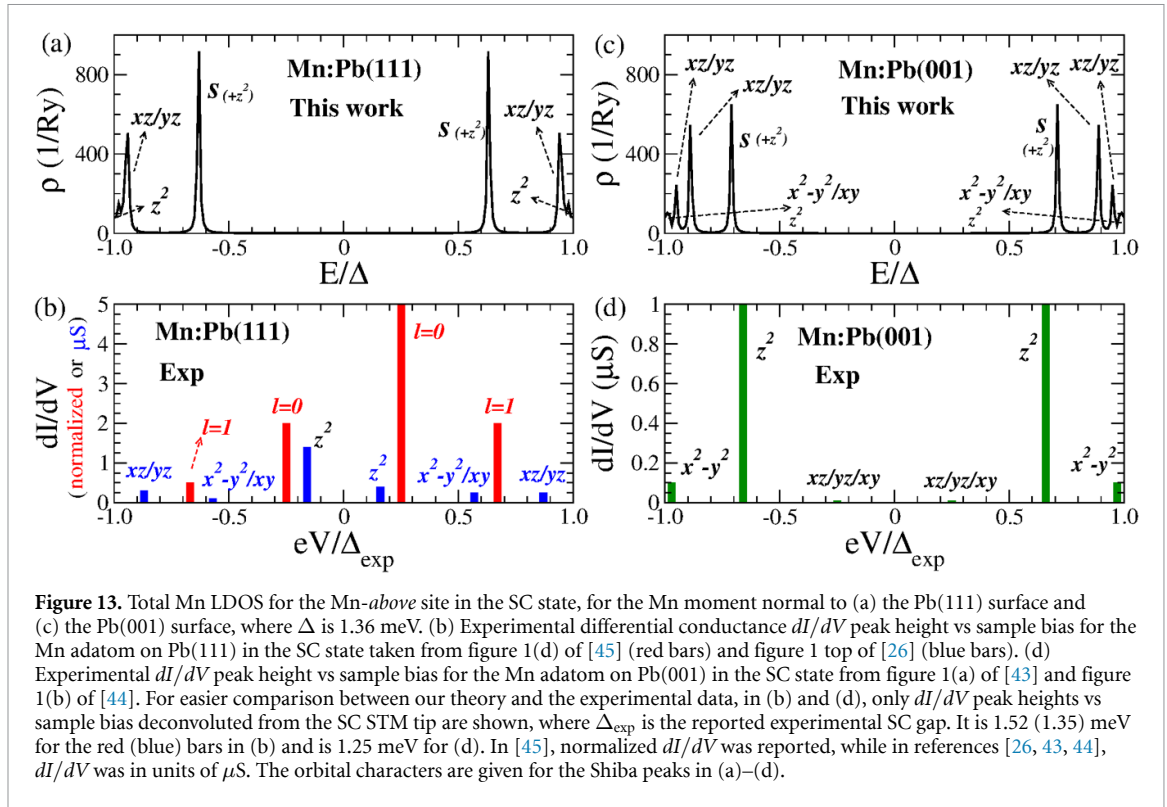
Regarding Pb(111) and Pb(001) surfaces, there exist several experimental studies of Shiba states from single Mn adatoms [26, 43–45] using SC STM tips. (In our work, we studied Fe, Co, and Mn adatoms on Pb(110) with an intention of examining dimers and longer chains on Pb(110) in the future which were experimentally studied.) Different surface orientations have different point group symmetries which play an important role in Shiba states. Therefore, we calculate Shiba states of a Mn adatom on Pb(111) and Pb(001) in the presence of SOC, when the magnetic moment of the Mn adatom points normal to each surface, using the same methods discussed in section 2. Then we compare our calculated Shiba states with the corresponding experimental results, assuming that experimental differential conductance, dI/dV, is proportional to calculated LDOS of the adatoms. In our theory, effects of the SC STM tips are not included. Note that the SC gap of Pb, Δ, is 1.36 meV in our calculations. Therefore, differences between the experimental energies and the calculated energies of the Shiba states are of an order of 0.1 meV.

6.1. Mn adatom on Pb(111)
We compute the Shiba states of the Mn adatom on a Pb(111) surface. Our calculation shows three pairs of Shiba states within the gap (figure 13(a)). The Shiba peaks near the gap have d_{z^2}-orbital character, while the deepest Shiba peaks have mainly s-orbital character with a small contribution from d_{z^2} orbital. The other Shiba peaks appearing at $\pm 0.94\Delta$ have d_{xz} and d_{yz} orbital characters. The orbital characterization is consistent with the point group symmetry of the (111) surface, C_{3v}.

Experimental STM data [45] showed two pairs of Shiba states labeled as $l = 0$ and $l = 1$ peaks (red bars in figure 13(b)). Another experimental STM data [26, 43] showed three pairs of Shiba states identified as $d_{xz,yz}$, $d_{x^2-y^2,xy}$, and d_{z^2} orbital contributions (blue bars in figure 13(b)). The Shiba peaks from the two experimental data have some similarities and some differences. The Shiba peaks in [45] are shown at $\pm 0.38(\pm 0.02)$ and $\pm 1.02(\pm 0.02)$ meV, while the peaks in [26] appear at ± 0.22, ± 0.77, and ± 1.18 meV. For easier comparison to our results, the experimental energies of the Shiba states in figure 13(b) are normalized by the SC gap, 1.52 (1.35) meV, as reported in [45] ([26, 43]).

First of all, some calculated Shiba peaks with $d_{xz,yz}$ and $\{s, d_{z^2}\}$ orbital characters (figure 13(a)) are also found in the experimental data [26, 43, 45]. In our calculation, however, the Shiba states of $d_{x^2-y^2}$ and d_{xy} character found in one of the experiments [43] do not appear within the SC gap. The energies of the deepest Shiba pair are quite different between our theory and the two experimental data. The most noticeable discrepancy between our theory and the experiments is the asymmetry in the experimental Shiba peak heights relative to the Fermi level (i.e. zero). It was proposed that the asymmetry in the spectral density occurs when on-site Coulomb interaction of the adatom (or non-magnetic potential scattering by the adatom) is greater than the SC gap [4]. For a normal STM tip, it was theoretically shown [46] that the dI/dV peak heights become asymmetric when the magnetic impurity interacts with other impurities or a normal reservoir. For a SC STM tip, a theory for the asymmetry was proposed in [26].

Figure 13. Total Mn LDOS for the Mn-*above* site in the SC state, for the Mn moment normal to (a) the Pb(111) surface and (c) the Pb(001) surface, where Δ is 1.36 meV. (b) Experimental differential conductance dI/dV peak height vs sample bias for the Mn adatom on Pb(111) in the SC state taken from figure 1(d) of [45] (red bars) and figure 1 top of [26] (blue bars). (d) Experimental dI/dV peak height vs sample bias for the Mn adatom on Pb(001) in the SC state from figure 1(a) of [43] and figure 1(b) of [44]. For easier comparison between our theory and the experimental data, in (b) and (d), only dI/dV peak heights vs sample bias deconvoluted from the SC STM tip are shown, where Δ_{exp} is the reported experimental SC gap. It is 1.52 (1.35) meV for the red (blue) bars in (b) and is 1.25 meV for (d). In [45], normalized dI/dV was reported, while in references [26, 43, 44], dI/dV was in units of μS. The orbital characters are given for the Shiba peaks in (a)–(d).

6.2. Mn adatom on Pb(001)

Now we discuss the case of a Mn adatom on Pb(001) in the SC state. Our calculation shows four pairs of Shiba states within the gap (figure 13(c)). The Shiba peaks near the gap have contributions from three orbitals such as $d_{x^2-y^2}$, d_{xy}, and d_{z^2}. The (001) surface has C_{4v} symmetry. The orbitals belonging to different irreducible representations are hybridized due to strong SOC. Two split pairs of Shiba states of d_{xz} and d_{yz} hybridized orbitals are found. The deepest pair of Shiba states have mainly s orbital character with a small d_{z^2}-orbital contribution.

The experimental energies of the Shiba states are ± 0.31, ± 0.82, and ± 1.21 meV that are normalized by the reported SC gap, 1.25 meV [43, 44]. Two of the four Shiba pairs such as $d_{x^2-y^2}$-orbital and s-orbital characters are also found in the experimental data (figure 13(d) [43, 44]) even with almost the same energies as the calculated values, if we allow a possibility of hybridization between d_{z^2} and s orbitals. Interestingly, for the Pb(001) surface, the experimental Shiba peak heights (dI/dV values) are symmetric relative to the Fermi level just like our calculated LDOS values. Again, the experimental deepest Shiba states appear much closer to the Fermi level than the calculated states.

7. Conclusions

We studied Shiba states of Fe, Co, and Mn adatoms on Pb(110) and a Mn adatom on Pb(111) and Pb(001) by using fully relativistic first-principles calculations including the band structure of the Pb substrate and all orbitals of the adatoms in the normal and SC states. In the normal state, the LDOS at the Fermi level is the highest (lowest) for the Co (Mn) adatom, while the spin moment of the adatom has an opposite trend.

For the Fe or Co adatom, five or six pairs of the Shiba states were spread out within the SC gap. Due to strong SOC of the Pb surface, the Shiba states cannot be characterized by separate orbitals categorized by irreducible representations of the point group but by J and m_J. Another hallmark of the SOC effect is that the Shiba states greatly change when the orientation of the adatom magnetic moment varies. By using a spin-polarized STM tip, the orientation of the adatom moment may be rotated within a surface plane.

Additionally, the deepest pair of the Shiba states can be merged to form a zero-energy state with the rotation of the adatom moment, whether the Fe or Co adatom is located above the surface or at the surface. Interestingly, this zero-energy state is found to be so fragile that it can be easily destroyed by an additional non-magnetic adatom right next to the magnetic adatom, although the other Shiba states remain unchanged. This kind of fragility test may be performed in STM experiments. This zero-energy state seems to be similar to the zero-bias peaks observed in Fe impurities on SC Ta(100)-(3×3)O [17], in magnetic molecules on a SC

Pb substrate [47, 48], in impurities on SC vanadium [49], and in Gd dimers/trimers in Bi-coated SC Nb [50], although their origins differ from our case.

For the Mn adatom on Pb(110), we show that all Shiba states are observed quite far from the zero energy, independently of the orientation of the moment. This is attributed to the tiny LDOS at the Fermi level, despite the largest Mn spin moment among the three adatoms. Therefore, we do not expect formation of a zero-energy state from the rotation of the Mn moment unless the LDOS at the Fermi level becomes significant.

Compared to the experimental data on Mn adatoms [26, 43–45], overall our Shiba states are in good agreement with experimental Shiba states. Our Shiba states show a significant dependence on the surface orientation, similarly to the experiments. Some calculated Shiba states are also found in the experimental data with the similar orbital characteristics and/or similar energies. There are, however, two small discrepancies between our theory and the experimental data for both Pb(111) and Pb(001). Firstly, the experimental deepest Shiba states [26, 43–45] appear much closer to the Fermi level than the calculated Shiba states. We cautiously speculate that this may be due to a large charge transfer between the adatom and the substrate in the experimental samples, which could increase the normal-state LDOS value at the Fermi level, similarly to figures 12(d)–(f). Secondly, the Shiba states with strong s-orbital character have not been identified in references [26, 43, 44], although it was reported for [45].

In order to further compare with experiments, we propose the following first-principles calculations/developments. Firstly, it would be interesting to compute a spatial distribution of the Shiba states along different k directions and compare it to experiments, similarly to references [51–54]. The experimental dI/dV intensity was shown to oscillate with a periodicity of 5.8 Å, for the Shiba states from the Mn adatom on Pb(111) [43]. Secondly, it would be useful to compute the Shiba states with either varying the vertical distances continuously, or varying the charge state of the adatom. Experimental data from different groups show somewhat different Shiba states even for the same Mn adatoms on the same Pb surface orientation [26, 43, 45]. As [43] pointed out, this is likely due to different vertical heights of the adatoms from the surface. The vertical height from the surface determines an amount of hybridization between the adatom and the substrate states. In addition, it can affect the charge state of the adatom via charge transfer between the adatom and the substrate [55, 56]. Thirdly, it would be interesting to compute the Shiba states for dimers (with different distances between them) and longer chains on Pb surfaces with noncollinear magnetism and study effects of canting and noncollinear magnetism on the Shiba states in long magnetic atomic chains.

Data availability statement

The data cannot be made publicly available upon publication because they are not available in a format that is sufficiently accessible or reusable by other researchers. The data that support the findings of this study are available upon reasonable request from the authors.

Acknowledgments

ORCID iDs

Kyungwha Park ⓘ https://orcid.org/0000-0002-0597-204X
Bendeguz Nyari ⓘ https://orcid.org/0000-0001-5524-9995
Andras Laszloffy ⓘ https://orcid.org/0000-0001-9863-3647

References

[1] Luh Y 1965 *Acta Phys. Sin.* **21** 75
[2] Shiba H 1968 *Prog. Theor. Phys.* **40** 435–51
[3] Rusinov A I 1969 *JETP Lett. (USSR)* **9** 85 (Engl. Transl.)

[4] Salkola M I, Balatsky A V and Schrieffer J R 1997 *Phys. Rev. B* **55** 12648–61

[5] Balatsky A V, Vekhter I and Zhu J X 2006 *Rev. Mod. Phys.* **78** 373–433

[6] Liebhaber E, Acero González S, Baba R, Reecht G, Heinrich B W, Rohlf S, Rossnagel K, von Oppen F and Franke K J 2020 *Nano Lett.* **20** 339–44

[7] Kuzmanovski D, Souto R S and Balatsky A V 2020 *Phys. Rev. B* **101** 094505

[8] Klinovaja J, Stano P, Yazdani A and Loss D 2013 *Phys. Rev. Lett.* **111** 186805

[9] Pientka F, Glazman L I and von Oppen F 2013 *Phys. Rev. B* **88** 155420

[10] Ruby M, Pientka F, Peng Y, von Oppen F, Heinrich B W and Franke K J 2015 *Phys. Rev. Lett.* **115** 197204

[11] Li J, Jeon S, Xie Y, Yazdani A and Bernevig B A 2018 *Phys. Rev. B* **97** 125119

[12] Nadj-Perge S, Drozdov I K, Li J, Chen H, Jeon S, Seo J, MacDonald A H, Bernevig B A and Yazdani A 2014 *Science* **346** 602–7

[13] Jeon S, Xie Y, Li J, Wang Z, Bernevig B A and Yazdani A 2017 *Science* **358** 772–6

[14] Feldman B E, Randeria M T, Li J, Jeon S, Xie Y, Wang Z, Drozdov I K, Andrei Bernevig B and Yazdani A 2017 *Nat. Phys.* **13** 286–91

[15] Pawlak R, Kisiel M, Klinovaja J, Meier T, Kawai S, Glatzel T, Loss D and Meyer E 2016 *npj Quantum Inf.* **2** 16035

[16] Ruby M, Heinrich B W, Peng Y, von Oppen F and Franke K J 2017 *Nano Lett.* **17** 4473–7

[17] Cornils L, Kamlapure A, Zhou L, Pradhan S, Khajetoorians A A, Fransson J, Wiebe J and Wiesendanger R 2017 *Phys. Rev. Lett.* **119** 197002

[18] Schneider L, Beck P, Neuhaus-Steinmetz J, Rózsa L, Posske T, Wiebe J and Wiesendanger R 2022 *Nat. Nanotechnol.* **17** 384–9

[19] Schneider L, Beck P, Posske T, Crawford D, Mascot E, Rachel S, Wiesendanger R and Wiebe J 2021 *Nat. Phys.* **17** 943–8

[20] Kuster F, Brinker S, Hess R, Loss D, Parkin S S P, Klinovaja J, Lounis S and Sessi P 2022 *Proc. Natl Acad. Sci.* **119** e2210589119

[21] Schneider L, Beck P, Wiebe J and Wiesendanger R 2021 *Sci. Adv.* **7** eabd7302

[22] Morr D K and Stavropoulos N A 2003 *Phys. Rev. B* **67** 020502

[23] Flatté M E and Reynolds D E 2000 *Phys. Rev. B* **61** 14810–4

[24] Vazifeh M M and Franz M 2013 *Phys. Rev. Lett.* **111** 206802

[25] Christensen M H, Schecter M, Flensberg K, Andersen B M and Paaske J 2016 *Phys. Rev. B* **94** 144509

[26] Ruby M, Pientka F, Peng Y, von Oppen F, Heinrich B W and Franke K J 2015 *Phys. Rev. Lett.* **115** 087001

[27] Arrachea L 2021 *Phys. Rev. B* **104** 134515

[28] Kim Y, Zhang J, Rossi E and Lutchyn R M 2015 *Phys. Rev. Lett.* **114** 236804

[29] von Oppen F and Franke K J 2021 *Phys. Rev. B* **103** 205424

[30] Ptok A, Głodzik S and Domański T 2017 *Phys. Rev. B* **96** 184425

[31] Brydon P M R, Das Sarma S, Hui H Y and Sau J D 2015 *Phys. Rev. B* **91** 064505

[32] Chiu C K and Wang Z 2022 *Phys. Rev. Lett.* **128** 237001

[33] Nyári B, Lászlóffy A, Szunyogh L, Csire G, Park K and Ujfalussy B 2021 *Phys. Rev. B* **104** 235426

[34] Beck P, Schneider L, Rózsa L, Palotás K, Lászlóffy A, Szunyogh L, Wiebe J and Wiesendanger R 2021 *Nat. Commun.* **12** 2040

[35] Saunderson T G, Annett J F, Csire G and Gradhand M 2022 *Phys. Rev. B* **105** 014424

[36] Lykken G I, Geiger A L, Dy K S and Mitchell E N 1971 *Phys. Rev. B* **4** 1523–30

[37] Csire G, Újfalussy B, Cserti J and Győrffy B 2015 *Phys. Rev. B* **91** 165142

[38] Vosko S H, Wilk L and Nusair M 1980 *Can. J. Phys.* **58** 1200–11

[39] Ebert H, Freyer H, Vernes A and Guo G Y 1996 *Phys. Rev. B* **53** 7721–6

[40] Lazarovits B, Szunyogh L and Weinberger P 2002 *Phys. Rev. B* **65** 104441

[41] Csire G, Deák A, Nyári B, Ebert H, Annett J F and Újfalussy B 2018 *Phys. Rev. B* **97** 024514

[42] Moca C P, Demler E, Jankó B and Zaránd G 2008 *Phys. Rev. B* **77** 174516

[43] Ruby M, Peng Y, von Oppen F, Heinrich B W and Franke K J 2016 *Phys. Rev. Lett.* **117** 186801

[44] Ruby M, Heinrich B W, Peng Y, von Oppen F and Franke K J 2018 *Phys. Rev. Lett.* **120** 156803

[45] Ji S H, Zhang T, Fu Y S, Chen X, Ma X C, Li J, Duan W H, Jia J F and Xue Q K 2008 *Phys. Rev. Lett.* **100** 226801

[46] Martin I and Mozyrsky D 2014 *Phys. Rev. B* **90** 100508

[47] Hatter N, Heinrich B W, Ruby M, Pascual J I and Franke K J 2015 *Nat. Commun.* **6** 8988

[48] Farinacci L, Ahmadi G, Reecht G, Ruby M, Bogdanoff N, Peters O, Heinrich B W, von Oppen F and Franke K J 2018 *Phys. Rev. Lett.* **121** 196803

[49] Huang H, Drost R, Senkpiel J, Padurariu C, Kubala B, Yeyati A L, Cuevas J C, Ankerhold J, Kern K and Ast C R 2020 *Commun. Phys.* **3** 199

[50] Ding H, Hu Y, Randeria M T, Hoffman S, Deb O, Klinovaja J, Loss D and Yazdani A 2021 *Proc. Natl Acad. Sci.* **118** e2024837118

[51] Menard G C *et al* 2015 *Nat. Phys.* **11** 1013–6

[52] Choi D J, Fernández C G, Herrera E, Rubio-Verdú C, Ugeda M M, Guillamón I, Suderow H, Pascual J I and Lorente N 2018 *Phys. Rev. Lett.* **120** 167001

[53] Park S *et al* 2021 *Nat. Commun.* **12** 4668

[54] Ortuzar J, Trivini S, Alvarado M, Rouco M, Zaldivar J, Yeyati A L, Pascual J I and Bergeret F S 2022 *Phys. Rev. B* **105** 245403

[55] Donati F *et al* 2021 *Nano Lett.* **21** 8266–73

[56] Tosoni S and Pacchioni G 2022 *Phys. Chem. Chem. Phys.* **24** 15891–903